Roles of Meridional Overturning in Subpolar Southern Ocean SST Trends: Insights from Ensemble Simulations

LIPING ZHANG,[a,b] THOMAS L. DELWORTH,[a] SARAH KAPNICK,[a] JIE HE,[c] WILLIAM COOKE,[a] ANDREW T. WITTENBERG,[a] NATHANIEL C. JOHNSON,[a] ANTHONY ROSATI,[a,b] XIAOSONG YANG,[a] FEIYU LU,[a,d] MITCHELL BUSHUK,[a,b] COLLEEN MCHUGH,[e] HIROYUKI MURAKAMI,[a,b] FANRONG ZENG,[a] LIWEI JIA,[a,b] KAI-CHIH TSENG,[a,d] AND YUSHI MORIOKA[f]

[a] *NOAA/Geophysical Fluid Dynamics Laboratory, Princeton, New Jersey*
[b] *University Corporation for Atmospheric Research, Boulder, Colorado*
[c] *School of Earth and Atmospheric Sciences, Georgia Institute of Technology, Atlanta, Georgia*
[d] *Program in Atmospheric and Oceanic Sciences, Princeton University, Princeton, New Jersey*
[e] *Science Applications International Corporation (SAIC), Reston, Virginia*
[f] *Application Laboratory, Research Institute for Value-Added-Information Generation (VAiG), JAMSTEC, Yokohama, Japan*

(Manuscript received 17 June 2021, in final form 16 November 2021)

ABSTRACT: One of the most puzzling observed features of recent climate has been a multidecadal surface cooling trend over the subpolar Southern Ocean (SO). In this study we use large ensembles of simulations with multiple climate models to study the role of the SO meridional overturning circulation (MOC) in these sea surface temperature (SST) trends. We find that multiple competing processes play prominent roles, consistent with multiple mechanisms proposed in the literature for the observed cooling. Early in the simulations (twentieth century and early twenty-first century) internal variability of the MOC can have a large impact, in part due to substantial simulated multidecadal variability of the MOC. Ensemble members with initially strong convection (and related surface warming due to convective mixing of subsurface warmth to the surface) tend to subsequently cool at the surface as convection associated with internal variability weakens. A second process occurs in the late-twentieth and twenty-first centuries, as weakening of oceanic convection associated with global warming and high-latitude freshening can contribute to the surface cooling trend by suppressing convection and associated vertical mixing of subsurface heat. As the simulations progress, the multidecadal SO variability is suppressed due to forced changes in the mean state and increased oceanic stratification. As a third process, the shallower mixed layers can then rapidly warm due to increasing forcing from greenhouse gas warming. Also, during this period the ensemble spread of SO SST trend partly arises from the spread of the wind-driven Deacon cell strength. Thus, different processes could conceivably have led to the observed cooling trend, consistent with the range of possibilities presented in the literature. To better understand the causes of the observed trend, it is important to better understand the characteristics of internal low-frequency variability in the SO and the response of that variability to global warming.

KEYWORDS: Climate variability; Southern Ocean

1. Introduction

The Southern Ocean (SO) distributes climate signals among the Atlantic, Pacific, and Indian Ocean Basins through its strong and eastward flowing Antarctic Circumpolar Current (ACC) (Fig. 1a), which plays a fundamental role in our climate system. In the current paper, we define the SO as the area south of 50°S, mainly referring to the subpolar region. The dynamics in the SO associated with the transformation of upwelled deep waters into dense Antarctic Bottom Water (AABW) or lighter intermediate and mode waters are critical components of the global meridional overturning circulation (MOC) (e.g., Orsi et al. 1999; Lumpkin and Speer 2007; Purkey and Johnson 2012; Marshall and Speer 2012; Fig. 1b). The wind-driven upwelling of deep water to the ocean surface and its subsequent transformation to lighter intermediate and mode waters or dense AABW feeds the upper and lower limbs of the MOC. The MOC plays a major role in moderating the climate system through its influences on the storage of anthropogenic heat and carbon (e.g., Sigman and Boyle 2000; Russell et al. 2006; Marshall and Speer 2012; He et al. 2017).

Given the importance of SO in the climate system, changes in SO properties observed since the beginning of the satellite era have received substantial attention. Interestingly, SSTs in the SO showed a small but significant cooling trend over the period 1980–2015 (e.g., Armour et al. 2016; Zhang et al. 2019). Accordingly, Antarctic sea ice showed an overall expansion trend (e.g., Turner et al. 2015). A period of anomalous warming and sea ice decrease was observed over the SO in 2016–17 (Parkinson 2019) associated with the formation of the Maud Rise Polynya (e.g., Campbell et al. 2019; Cheon and Gordon 2019). Despite this anomalous warming, Chemke and Polvani (2020) pointed out that the Antarctic sea ice extent still exhibited a modest increasing trend during the 1980–2019 period. Most model simulations exhibit strong warming and substantial sea ice decline over these periods (e.g., Turner et al. 2015; Chemke and Polvani 2020; Roach et al. 2020).

Supplemental information related to this paper is available at the Journals Online website: https://doi.org/10.1175/JCLI-D-21-0466.s1.

Corresponding author: Liping Zhang, liping.zhang@noaa.gov

DOI: 10.1175/JCLI-D-21-0466.1

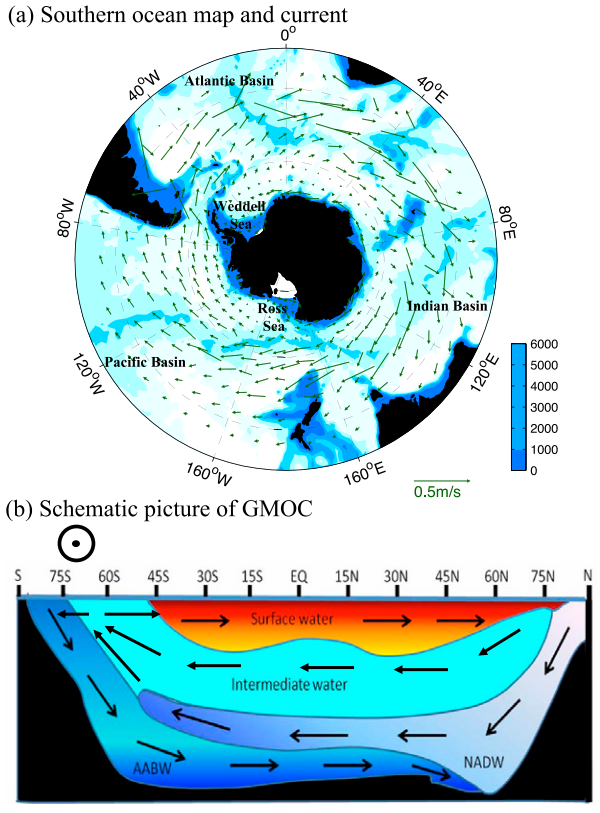

FIG. 1. (a) Simulated Southern Ocean bathymetry (shading is ocean depth in m) and surface current at 10 m (green vectors) calculated from the GFDL SPEAR_MED control simulation. (b) Schematic picture of the upper cell and low cell of the global meridional overturning circulation (GMOC). Orange and light blue colors denote the lighter surface and intermediate waters. The blue and purple colors denote the North Atlantic Deep Water (NADW) and Antarctic Bottom Water (AABW), emanating from, respectively, northern and southern polar seas. The target shape in (b) denotes Southern Ocean westerlies blowing from west to east.

Several hypotheses have been proposed to explain the SO cooling trend, including 1) surface wind changes driven by the southern annular mode (SAM) (e.g., Turner et al. 2009; Holland and Kwok 2012) or the tropical Pacific and North Atlantic SST anomalies (Li et al. 2014; Meehl et al. 2016; Purich et al. 2016; Lee et al. 2017), 2) SO surface freshening caused by anthropogenic warming or northward sea ice freshwater transport (e.g., de Lavergne et al. 2014; Bintanja et al. 2013; Bronselaer et al. 2018; Haumann et al. 2016), 3) natural internal variability (e.g., Polvani and Smith 2013; Zhang et al. 2019; Singh et al. 2019), 4) ocean heat transport by SO background MOC (e.g., Armour et al. 2016), and 5) the role of ocean mesoscale processes (Bilgen and Kirtman 2020). It is a significant challenge to models to represent all of these processes realistically, and deficiencies in these representations likely contribute to the inability of most models to capture the observed cooling SST trend. These proposed mechanisms are not completely independent from one another but are linked by their suggestion of the importance of changes in vertical convection and thus an altered MOC in explaining the observed trends. For example, the suppression of vertical convection by surface freshening prevents the mixing of warm subsurface water toward the ocean surface, leading to declining SSTs. This reduced convection is linked to a reduction in the strength of the lower limb of the MOC. A particular phase of low-frequency variability associated with reduced SO convection (occurring after the peak phase of convection) and the lower limb of the MOC may explain recent observed SO trends (Zhang et al. 2019). Again, this hypothesis highlights the important role of the bottom limb of MOC, although the convection weakening is due to internal variability in their study. These hypotheses centered on convection weakening tend to be supported by the subsurface ocean observation, since the SO subsurface shows a warming temperature trend and there is a global contraction of AABW between the 1980s and 2000s (e.g., Purkey and Johnson 2012, 2013). Armour et al. (2016) further argued that more heat storage occurs along the northern flank of the ACC than south of it due to the northward transport of the anomalous heat by the mean wind-driven MOC. All of these mechanisms to explain the observed trends in the SO have been derived using diverse methods and various climate models. This raises the natural question: are these hypotheses independent from one another or is it possible that they all are contributing to the observed trends? We use the results from a large ensemble of climate change experiments to provide a more unified picture of these hypotheses. Specifically, we explore three questions: 1) What is the role of internal variability in determining modeled SST trends in the SO? 2) Does enhanced surface freshening in response to anthropogenic forcing lead to reduced convection which may contribute to the recent SO SST trend? 3) What role does upwelling in the SO play in modulating SSTs when the lower limb of the MOC is suppressed as a result of increased radiative forcing?

2. Models and large-ensemble experiments

The large-ensemble simulations we analyzed in this study are based on the SPEAR_LO and SPEAR_MED models (SPEAR is Seamless System for Prediction and Earth System Research) recently developed at the National Oceanographic and Atmospheric Administration's (NOAA) Geophysical Fluid Dynamics Laboratory (GFDL) (Delworth et al. 2020). SPEAR_LO and SPEAR_MED have the same ocean and ice components, MOM6 and SIS2, as described in detail in Adcroft et al. (2019). The ocean component has a horizontal resolution of approximately 1° (100 km) in the subpolar and subtropical regions, with meridional refinement to 1/3° (40 km) in the tropics and 1/2° (30 km) in the polar oceans. There are 75 vertical layers in the ocean component. The atmospheric and land components of SPEAR come from the GFDL AM4-LM4 code (Zhao et al. 2018a,b). The horizontal resolution of the atmospheric/land model is approximately 100 km in SPEAR_LO and 50 km in SPEAR_MED. The

atmosphere component has 33 levels in the vertical with a model top of 1 hPa in both models.

We conduct Control simulations with atmospheric composition fixed at preindustrial levels (calendar year 1850) using SPEAR_LO and SPEAR_MED respectively. We also analyze large-ensemble simulations of SPEAR_LO and SPEAR_MED that cover the historical and twenty-first-century periods. The ensembles contain 30 members, with each member initialized from points in the control simulations that are 20 years apart in order to sample different phases of internal climate variability. The SPEAR_LO large-ensemble simulation covers calendar years from 1851 to 2100, while the SPEAR_MED has a shorter time length that extends from calendar year 1921 to 2100 because of the larger computational expense of its higher-resolution atmosphere component. The historical and twenty-first-century ensemble simulations are driven by the same natural and anthropogenic forcings used in historical (1850–2014) and Shared Socioeconomic Pathway (SSP) 5–8.5 (SSP5–8.5; Riahi et al. 2017) experiments (2015–2100) from phase 6 of the Coupled Model Intercomparison Project (CMIP6) (Eyring et al. 2016). We denote these ensembles with historical and future projected radiative forcings using SPEAR_LO and SPEAR_MED models as SPEAR_LO_SSP585 and SPEAR_MED_SSP585, respectively. Additional large ensembles, forced by median future projected radiation (SSP2–4.5) using SPEAR_MED, are denoted by SPEAR_MED_SSP245. To separate the roles of anthropogenic and natural forcings in climate variability and change, we also conduct large ensembles that driven only by natural forcings in both models; these are named SPEAR_LO_Natural and SPEAR_MED_Natural.

We also compare the results from SPEAR_LO and SPEAR_MED ensembles with those from the National Center for Atmospheric Research (NCAR) Community Earth System Model (CESM) (Kay et al. 2015; Kim et al. 2018) and previous GFDL SPEAR_AM2 and FLOR (Forecast-oriented Low Ocean Resolution) large ensembles (Zhang et al. 2019; Vecchi et al. 2014). The CESM large ensemble used here consists of 50 members, with 40 members started from different atmosphere initial conditions (Kay et al. 2015) and 10 members initialized using different ocean initial conditions (Kim et al. 2018). The CESM ensembles are driven by similar historical and future radiative forcings used in SPEAR. The SPEAR_AM2 large ensemble is the same as in SPEAR_LO, except that the atmosphere component uses the GFDL AM2-LM2 model (Anderson et al. 2004). In the FLOR ensemble, the atmosphere and land components are from the GFDL CM2.5 model (Delworth et al. 2012), while the ocean and sea ice components are based on the low-resolution GFDL CM2.1 model (Delworth et al. 2006). All models and experiments used in the present study are summarized in Table 1.

All models we used here have reasonable mean states over the SO (see the online supplemental material). The SO exhibits warm SST biases in all models (Fig. S1 in the online supplemental material), as is commonly found in other coupled climate models (e.g., Wang et al. 2014). The SST bias in SPEAR_MED and SPEAR_LO is much smaller compared to previous GFDL models. This is a big improvement for GFDL new-generation models (e.g., Delworth et al. 2020). In the subsurface ocean, the SPEAR_MED and SPEAR_LO also have the least temperature and salinity biases in all five models (Figs. S2 and S3). These improvements increase our confidence in the ability to use the SPEAR models to investigate the scientific questions posed in the introduction. We also note that the NCAR CESM model has a strong freshwater cap over the SO (Fig. S3g), corresponding to negative salinity biases over the upper ocean and a strong ocean stratification background.

3. SO MOC and SST variability in SPEAR models

Figures 2a–d show the long-term mean Global MOC (GMOC) in SPEAR_LO and SPEAR_MED control simulations in depth and density spaces, respectively. The negative streamfunction south of 60°S is an anticlockwise meridional cell, which is largely associated with the AABW formation and we refer to this hereafter as the AABW cell. In the 60°–40°S latitude band, there is a strong positive streamfunction in depth space (Figs. 2a,b), which represents the clockwise Deacon cell. Different from the largely thermohaline-driven AABW cell, the Deacon cell is mainly driven by SO westerly winds and therefore is much more obvious in depth space than in density space (Figs. 2a,b vs Figs. 2c,d). The SO westerly winds induce upwelling poleward of the zonal wind maximum and downwelling equatorward of the zonal wind maximum. This wind-induced water divergence and convergence trigger the meridional Deacon cell, which acts to steepen isopycnals, supporting the thermal wind transport of the ACC and creating a store of available potential energy (Marshall and Speer 2012). In this paper, we define the Deacon cell strength as the maximum streamfunction value within the 40°–60°S latitude band in depth space.

Similar to previous studies (e.g., Zhang and Delworth 2016; Zhang et al. 2019), we use the AABW cell, defined as the absolute value of minimum GMOC south of 60°S, as a proxy for the strength of SO deep convection. The long-term mean AABW cell strength in depth space is comparable in the SPEAR_LO and SPEAR_MED Control simulations, with values of 3.5 and 3.4 Sv (1 Sv $\equiv 10^6$ m^3 s^{-1}), respectively (Figs. 2a,b). The AABW cell strength increases to 24.8 and 25.2 Sv in the two models when calculated in density space (Figs. 2c,d), which are within observed estimates (21 $\pm$ 6 Sv) (Ganachaud and Wunsch 2000). Similar to the Atlantic meridional overturning circulation (AMOC) definition, the smaller AABW cell values in depth space arise because northward and southward transport of water with different density characteristics can occur at the same depth in z space, and therefore compensate each other in the same depth layer (Zhang 2010). Despite the magnitude of the differences of AABW cell in depth and density spaces, their associated time series in long control simulations covary with each other (correlation is about 0.85).

In SPEAR_LO and SPEAR_MED, the AABW cell variability is largely associated with deep convection fluctuations around the Ross Sea, whereas convective activity over the

TABLE 1. Description of models and large-ensemble experiments used in the current paper.

Name	General information	Model grids	Experiments	Reference
SPEAR_LO	Coupled model developed at GFDL. Ocean and Ice use MOM6-SIS2. Atmos and Land are from AM4-LM4.	Ocean and Ice: 1°, tropical (subpolar) refinement to 1/3° (1/2°), 75 vertical layers Atmos and Land: 100 km, 33 levels	Control run (fixed radiative forcing at 1850) Large ensembles (30 members, years 1851–2100): SPEAR_LO_SSP585 (historical and SSP5–8.5 forcing) SPEAR_LO_Natural (natural forcing)	Delworth et al. (2020) Adcroft et al. (2019) Zhao et al. (2018a,b)
SPEAR_MED	Same Ocean and Ice as SPEAR_LO, but AM4-LM4 has finer horizontal resolution.	Ocean and Ice: Same as SPEAR_LO Atmos and Land: 50 km; Atmos has 33 levels	Control run (fixed radiative forcing at 1850) Large ensembles (30 members, years 1921–2100): SPEAR_MED_SSP585 (historical and SSP5–8.5 forcing) SPEAR_MED_SSP245 (historical and SSP2–4.5 forcing) SPEAR_MED_Natural (natural forcing)	Delworth et al. (2020) Adcroft et al. (2019) Zhao et al. (2018a,b)
NCAR_CESM	Coupled model developed at NCAR. Ocean and Ice use POP2 and CICE4. Atmos and Land are from CAM5-CLM4.	Ocean and Ice: 1°; Ocean has 60 layers Atmos and Land: 1° (100 km); Atmos has 30 levels	Control run (fixed radiative forcing at 1850) Large ensembles (50 members, years 1921–2100): NCAE_CESM1_LE (historical and (SSP) 5–8.5 forcing)	Kay et al. (2015) Kim et al. (2018)
SPEAR_AM2	Coupled model developed at GFDL. Ocean and Ice use MOM6. Atmos and Land are from AM2-LM2.	Ocean and Ice: Same as SPEAR_LO and SPEAR_MED Atmos and Land: 200 km	Control run (fixed radiative forcing at 1850) Large ensembles (30 members, years 1851–2100): SPEAR_AM2_SSP585 (historical and (SSP) 5–8.5 forcing) SPEAR_AM2_Natural (natural forcing)	Zhang et al. (2019)
FLOR	Coupled model developed at GFDL. Ocean and Ice use MOM4. Atmos and Land are from AM2-LM2.	Ocean and Ice: 1°, Atmos and Land: 50 km	Control run (fixed radiative forcing at 1850) Large ensembles (30 members, years 1921–2100): FLOR_RCP85 (historical and RCP 8.5 forcing) FLOR_Natural (natural forcing)	Vecchi et al. (2014)

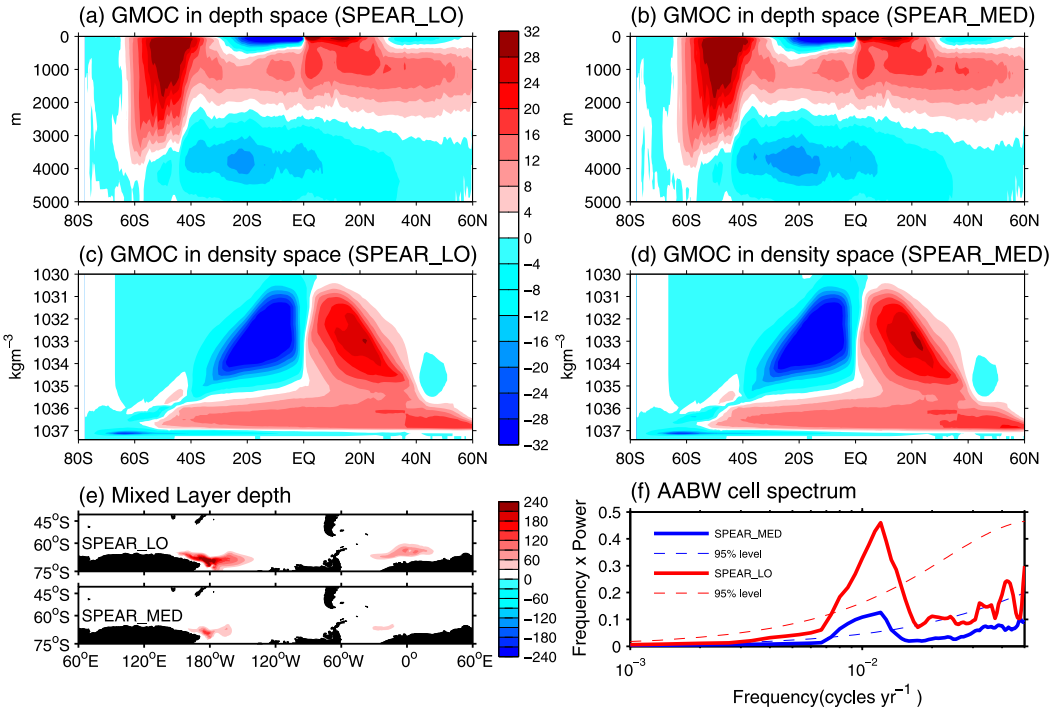

FIG. 2. Long-term mean global meridional overturning circulation (GMOC; Sv) streamfunction in (a),(c) SPEAR_LO and (b),(d) SPEAR_MED control simulations calculated in (a),(b) depth space and (c),(d) density space, respectively. The GMOC is calculated using the mean plus eddy-induced velocities and thus represents the residual mean MOC. (e) Regression of annual mean mixed layer depth (MLD) against the Antarctic Bottom Water (AABW) cell index in these two models (m Sv^{-1}). The AABW cell index is defined as the absolute value of minimum streamfunction south of 60°S in depth space. The MLD is defined as the depth where the density difference between surface equals 0.03 kg m^{-3}. (f) Power spectrum of the AABW cell index in two models, along with their 95% confidence level.

Weddell Sea plays a secondary role [see the mixed layer depth (MLD) response in Fig. 2e]. SPEAR forms a large amount of AABW around the Ross Sea over the continental shelf, which is a notable improvement over previous GFDL models (Delworth et al. 2020). In contrast, the Weddell Sea convection is weaker and mainly occurs in the open ocean. This Weddell Sea convection increases the rate of AABW formation as observed during the 1974–76 Weddell Polynya (Gordon 1978; Martinson 1991). Compared to SPEAR_MED, the convection variability is stronger in SPEAR_LO in both the Ross and Weddell Seas (Fig. 2e). Power spectrum analysis further shows that the convective activity can fluctuate on centennial time scales, with a period around 100 years (Fig. 2f). The strength contrast is broadly seen in almost all frequency bands and has a maximum around 100 years (Fig. 2f). Zhang et al. (2021) suggested that the amplitude of SO convection variability can be associated with the size of the subsurface heat reservoir to the extent that the frequency of convection is controlled by conditions in the deep ocean. Moreover, increases of the subsurface heat reservoir can arise both from enhanced horizontal temperature advection and from enhanced ocean stratification. Here, we find the NADW and Antarctic circumpolar bottom waters in SPEAR_LO are much warmer than those in SPEAR_MED. The associated positive temperature advection by the subpolar gyre may increase the subsurface heat reservoir in the SO and therefore leads to a larger convection amplitude in the SPEAR_LO. This preliminary analysis needs to be examined carefully in the future.

To investigate how this internal SO convection variability evolves under natural and anthropogenic forcings and whether such a convection change can imprint on SST variability, we examine the time evolution of the AABW cell and SO SST (Fig. 3). The low-frequency SO convection fluctuations are clearly seen in each ensemble member, especially in the nineteenth and twentieth centuries (Figs. 3a,c,e). In contrast, the ensemble mean convection response follows a nearly horizontal line during the same period, indicating that changes in radiatively forced convection are negligible. Due to the larger internal convection variability in the SPEAR_LO control simulation (Fig. 2f), the convection spread across 30 members in SPEAR_LO_SSP585 is also larger than that in SPEAR_MED_SSP585 and SPEAR_MED_SSP245 during this stage (Figs. 3a,c,e). The SO SST evolution also shows substantial low-frequency variabilities (Figs. 3b,d,f). We show ensemble members 4 and 30 in

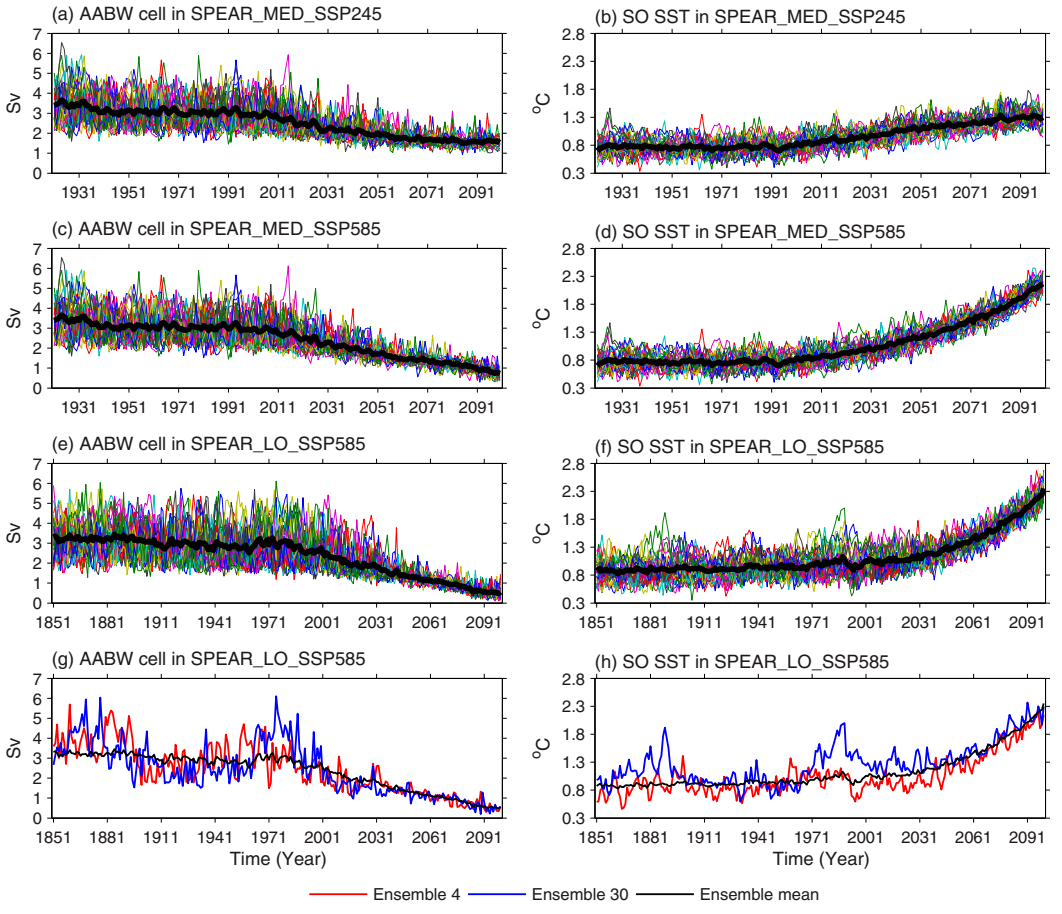

FIG. 3. Time evolutions of the (a),(c),(e) AABW cell (Sv) and (b),(d),(f) Southern Ocean (SO) area mean (south of 50°S) SST indices (°C) in the (a),(b) SPEAR_MED_SSP245, (c),(d) SPEAR_MED_SSP585, and (e),(f) SPEAR_LO_SSP585 large-ensemble simulations. Thick black lines denote the ensemble-mean time series, while other thin lines with different colors denote different ensemble members. (g),(h) The AABW cell and SO SST time series, respectively, in ensemble member 4 (red line) and ensemble member 30 (blue line), as well as the ensemble mean (black line) in SPEAR_LO_SSP585.

SPEAR_LO_SSP585 as an example (Figs. 3g,h). The internal low-frequency SO convection variability appears to strongly imprint on the SO SST, with stronger-than-normal convection corresponding to warmer-than-normal SST in most time periods and vice versa. Moreover, the SST ensemble spread in SPEAR_LO during this period is larger than that in SPEAR_MED (Fig. 3f vs Figs. 3b,d) because of stronger internal convection variability in the former model.

As we move into the twenty-first century, the amplitude of the internal convection variability and ensemble spread decrease (Figs. 3a,c,e). These are also accompanied with a weakening of the convection mean state. With a smaller radiative forcing in SPEAR_MED_SSP245, SO convection weakens less in terms of both spread and mean state compared to SPEAR_MED_SSP585 (Fig. 3a vs Fig. 3c). During some decades before and after year 2000, both the convection internal variability and forced convection weakening are clearly seen (Figs. 3a,c,e). In the last several decades of the twenty-first century, the convection mean state and variability are very small, indicating that SO convection is highly damped. Due to the different climate sensitivities in SPEAR_LO and SPEAR_MED, the strength of the AABW cell at the end of the twenty-first century is weaker in SPEAR_LO_SSP585 compared to SPEAR_MED_SSP585 despite being forced with the same radiative forcings (Fig. 3c vs Fig. 3e). The spread of convection across the ensemble members also seems smaller after year 2040 in SPEAR_LO_SSP585 compared to SPEAR_MED_SSP585, even though the internal convection amplitude is stronger in the former model. The SO SST shows a consistent warming trend, with a smaller (larger) warming in response to weaker (stronger) radiative forcings (Fig. 3b vs Fig. 3d). Again, the forced SST warming at the end of the twenty-first century differs between models due to different model sensitivities (Fig. 3d vs Fig. 3f).

Overall, the simulated SO convection experiences three different regimes when driven by the natural and anthropogenic forcings: the first stage (nineteenth and twentieth centuries) is dominated by internal convection fluctuations, and the second

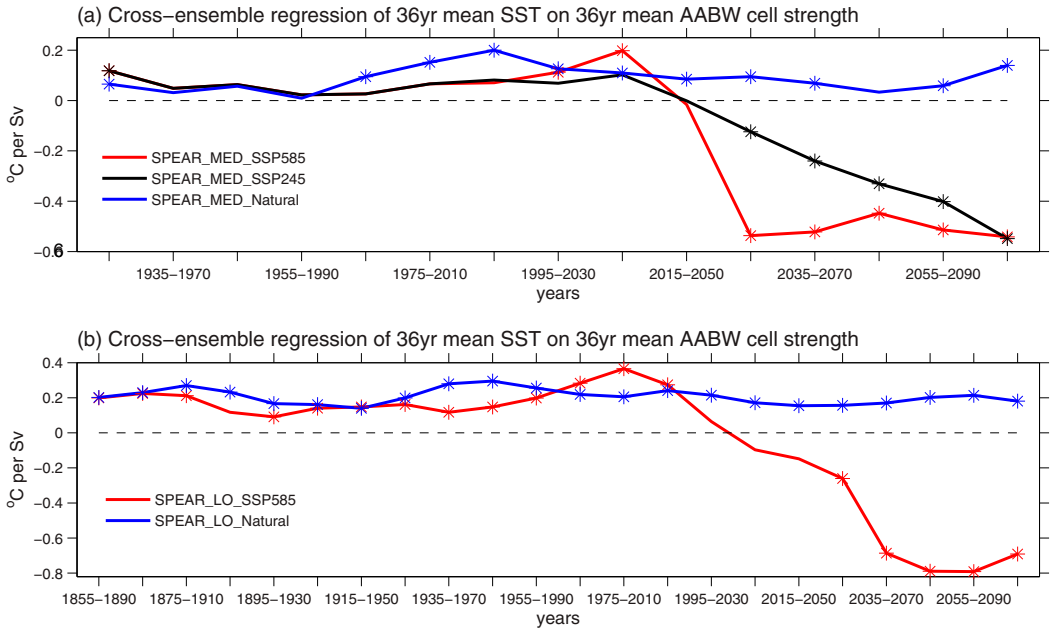

FIG. 4. (a) Cross-ensemble regression of 36-yr mean SO SST upon the 36-yr mean AABW cell strength in SPEAR_MED_SSP585 (red line), SPEAR_MED_SSP245 (black line), and SPEAR_MED_Natural (blue line) large ensembles (°C Sv^{-1}). This 36-yr window extends through the whole integration period with a time interval of 10 years. (b) As in (a), but for the SPEAR_LO_SSP585 and SPEAR_LO_Natural simulations. The asterisks indicate the regressions that are significant at a 90% confidence level based on a Student's *t* test.

stage (early twenty-first century) includes both internal variability and forced convection weakening; during the third stage (second half of the twenty-first century), the convective variability is damped, and the anthropogenic warming becomes dominant. These convection evolutions have the potential to impact SO SSTs and temporal trends. In the next sections, we explore the possible roles that SO convection plays in 36-yr trends in SO SSTs during different periods. When convection is strongly damped, we will examine the role that the Deacon cell associated with the SO upwelling plays in SO SSTs. A 36-yr time period is used for analysis given that observations show the most significant cooling trend over the time period 1980–2015.

4. Potential mechanisms of SST trends

a. The possible role of internal SO deep convection variability in SO SST trends

The time series of AABW cell strength and SST in Figs. 3g and 3h suggest that the internal SO convection variability can strongly imprint on SO SST in the nineteenth and twentieth centuries, even extending into the early twenty-first century. To better investigate this relationship, we conduct a cross-ensemble regression of 36-yr mean SO SST on the 36-yr mean AABW cell strength using the large-ensemble simulations (Fig. 4). The cross-ensemble regression is similar to the classic regression analysis except that the time dimension is replaced with different ensemble members. This 36-yr window is performed throughout the entire integration time with an interval of 10 years (1855–90, 1865–1900, … , 2065–2100). In the SPEAR_MED_Natural, we find positive regression coefficients throughout the entire simulation, with a stronger-than-normal SO convection corresponding to a higher-than-normal SO SST and vice versa. Since there are no anthropogenic forcings in the Natural run, the internal SO convection variability dominates in this experiment. The stronger-than-normal convection brings warm subsurface water to the surface and thus leads to anomalously warm SSTs. This positive relationship between SO convection and SST is broadly seen in control simulations of previous GFDL climate models (e.g., Zhang and Delworth 2016; Zhang et al. 2017). When anthropogenic forcings are included positive regression coefficients are still clearly seen before the 2015–50 time period in SPEAR_MED_SSP585 and SPEAR_MED_SSP245. After this period, however, the regression coefficients switch sign and become increasingly negative as the impacts of anthropogenic forcings grow (Fig. 4a). This inflection point indicates the end of the period in which internal variability processes dominate convection variability. In section 6, we will examine what possible processes control the negative regression coefficients after that inflection point. Similar phenomena are seen in the SPEAR_LO large ensemble (Fig. 4b), except that the positive regression coefficients are larger (Figs. 4a,b), mainly arising from the larger internal SO convection variability in Control simulation (Fig. 2f). This indicates that with the stronger internal SO convection variability in the SPEAR_LO Control simulation there is a stronger imprint

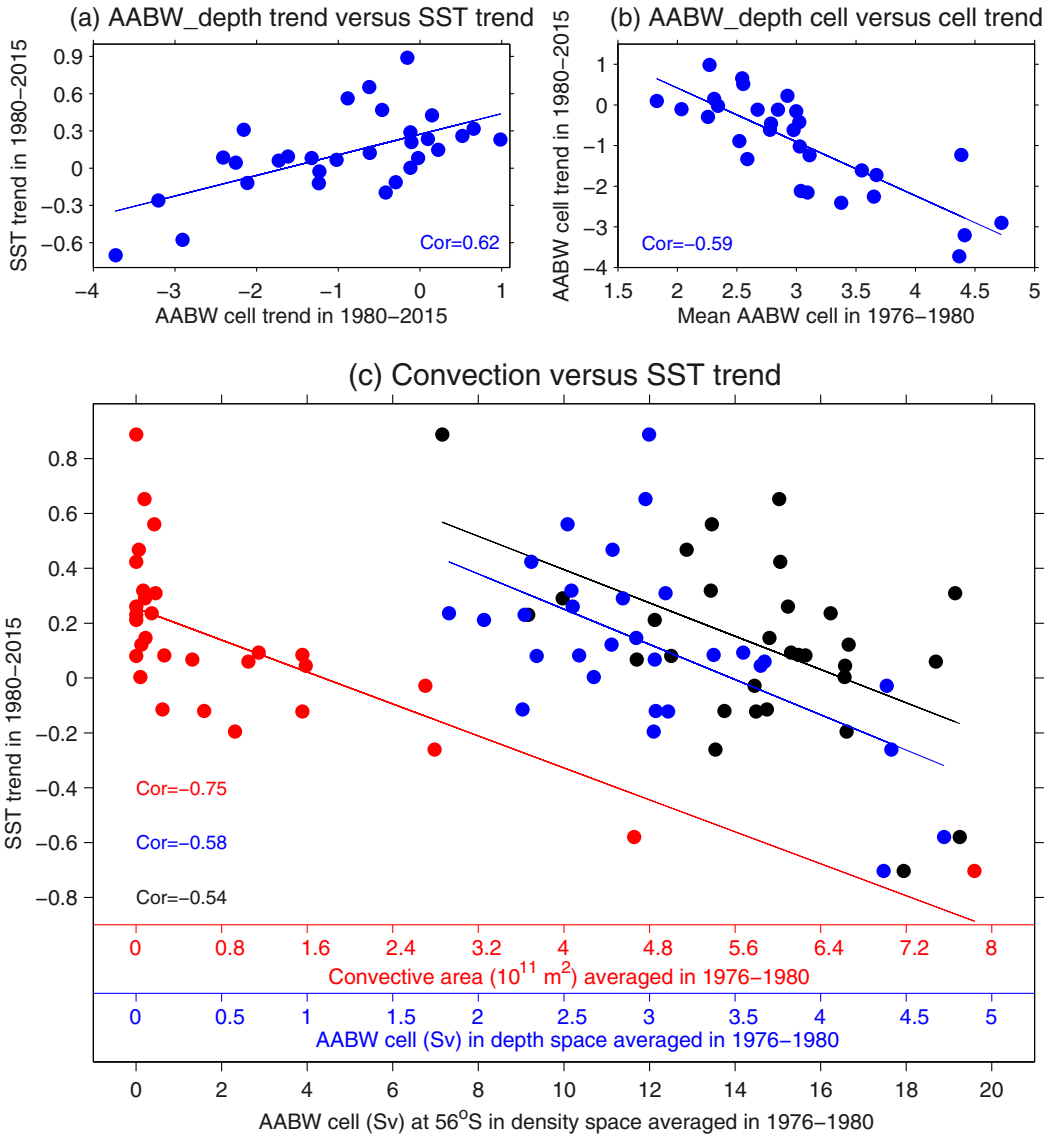

FIG. 5. (a) Scatterplot of annual mean AABW cell trend [in depth space; Sv (36 yr)$^{-1}$] vs annual mean SST trend [°C (36 yr)$^{-1}$] in years 1980–2015 in SPEAR_LO_SSP585 large ensembles. (b) As in (a), but for the mean AABW cell strength averaged in years 1976–80 (Sv) vs the annual mean AABW cell trend [Sv (36 yr)$^{-1}$] in years 1980–2015. (c) As in (a), but for the mean SO convection strength averaged in 1976–80 (Sv) vs the annual mean SO SST trend in years 1980–2015 [°C (36 yr)$^{-1}$]. The SO convection strength is represented by the AABW cell index in depth space (blue dots; Sv), in density space (black dots; Sv) and convection area where the September MLD exceeds 2000m (red dots; 10^{11} m^2). The lines in the panels denote the best linear fit according to least squares regression. The correlations are also shown in corners and all of them are significant at a 95% confidence level based on a Student's *t* test.

of that variability on the SO SST mean state in historical and future projection runs.

In addition to the mean state, the internal SO convection variability also affects the SO SST trend on decadal time scales. As an example, we show in Fig. 5 the SO convection strength versus annual mean SST trends in the recent period of 1980–2015 in SPEAR_LO_SSP585. The AABW cell trend is positively correlated with the SO SST trend across 30 ensemble members (Fig. 5a). The more the AABW cell strengthens, the more positive the SO SST trend is, and vice versa. Similar to the mean state response (Fig. 4), the increasing convection favors convective warming and thus causes a positive SST trend. Due to the long memory of the deep ocean, SO internal convection variability has a long persistence time scale that can be up to three decades (e.g., Zhang et al. 2017; Zhang et al. 2019). This decadal persistence is also seen from the large ensembles. Figure 5b shows that a stronger initial SO convection mean state in 1976–80 corresponds

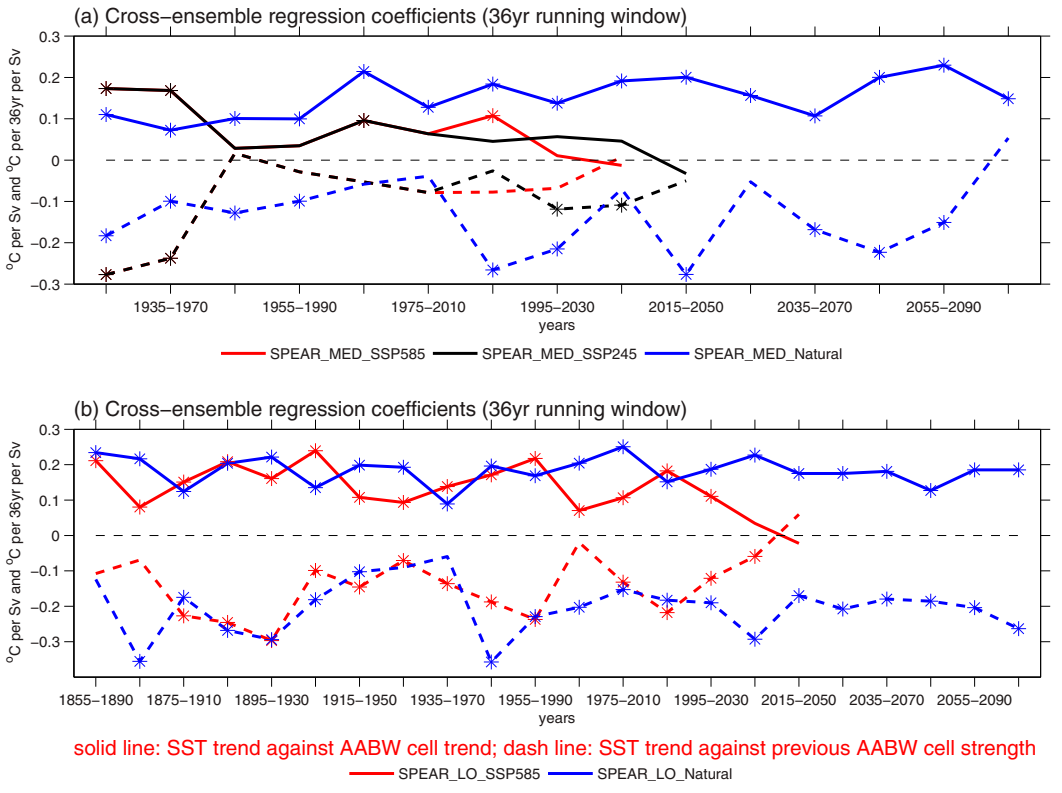

FIG. 6. (a) Cross-ensemble regression of 36-yr SO SST trend upon the 36-yr AABW cell strength trend (initial 5-yr-averaged AABW strength), denoted by solid (dashed) lines, in SPEAR_MED_SSP585 (red line), SPEAR_MED_SSP245 (black line), and SPEAR_MED_Natural (blue line) large ensembles. This 36-yr window extends through the whole integration period with a time interval of 10 years. (b) As in (a), but for the SPEAR_LO_SSP585 and SPEAR_LO_Natural simulations. Units are °C Sv^{-1} for the SST trend regression against the AABW cell trend and °C $(36\ yr)^{-1}$ Sv^{-1} for the SST trend regression against the initial AABW cell strength. The asterisks indicate the regressions that are significant at a 90% confidence level based on a Student's *t* test.

to a larger negative trend in convection over the following 36 years (1980–2015). Due to the positive correlation between AABW cell trend and SO SST trend, we then see a clearly negative relationship between the initial convection strength averaged in 1976–80 and the subsequent SO SST trend in 1980–2015 (Fig. 5c). It is worth noting that this relationship is robust no matter how we define SO convection strength. Here, we also define the convection strength as the total convection area south of 55°S where the September MLD exceeds 2000 m (red dots in Fig. 5c) as suggested by de Lavergne et al. (2014). All SO convection indexes (GMOC in depth space, in density space and convection area) show that the stronger (weaker) the initial SO convection state is, the more negative (positive) the SST trend is over the SO during the next 36 years. This phenomenon is consistent with the modeling results in Zhang et al. (2019), in which they initialize historical simulations using different SO convection states, and the observed SO cooling trend is simulated when starting from an active phase of SO convection.

Figure 6 further shows that the impact of internal SO convection variability on the SO SST trends is robust across various time periods and models. In the SPEAR_MED_Natural, the positive relationship between 36-yr AABW trend and 36-yr SO SST trend and the negative relationship between initial AABW strength and the subsequent 36-yr SO SST trend are clearly seen throughout the integration periods (Fig. 6a). However, the internal convection influence on the 36-yr SST trend only lasts to the approximate period of 2005–40 in SPEAR_MED_SSP585 and 2015–50 in SPEAR_MED_SSP245 (Fig. 6a). This is not surprising, since the internal SO convection variability persists in the whole integration period in the Natural run, while convection variability damps in later periods in the latter two experiments due to anthropogenic forcings (Figs. 3 and 4). The influence of internal convection variability disappears a little bit earlier in SPEAR_MED_SSP585 than in SPEAR_MED_SSP245 (Fig. 6a), presumably due to larger radiative forcing and the associated earlier damping of convection variability in the former experiment. Compared to SPEAR_MED, the regression coefficients of convection strength (trend or initial state) on the SO SST trend in SPEAR_LO are larger in both Natural and SSP runs (Fig. 6a vs Fig. 6b). This suggests that the internal SO convection variability imprints more on the SO 36-yr SST trend in SPEAR_LO large ensembles, which is again associated with

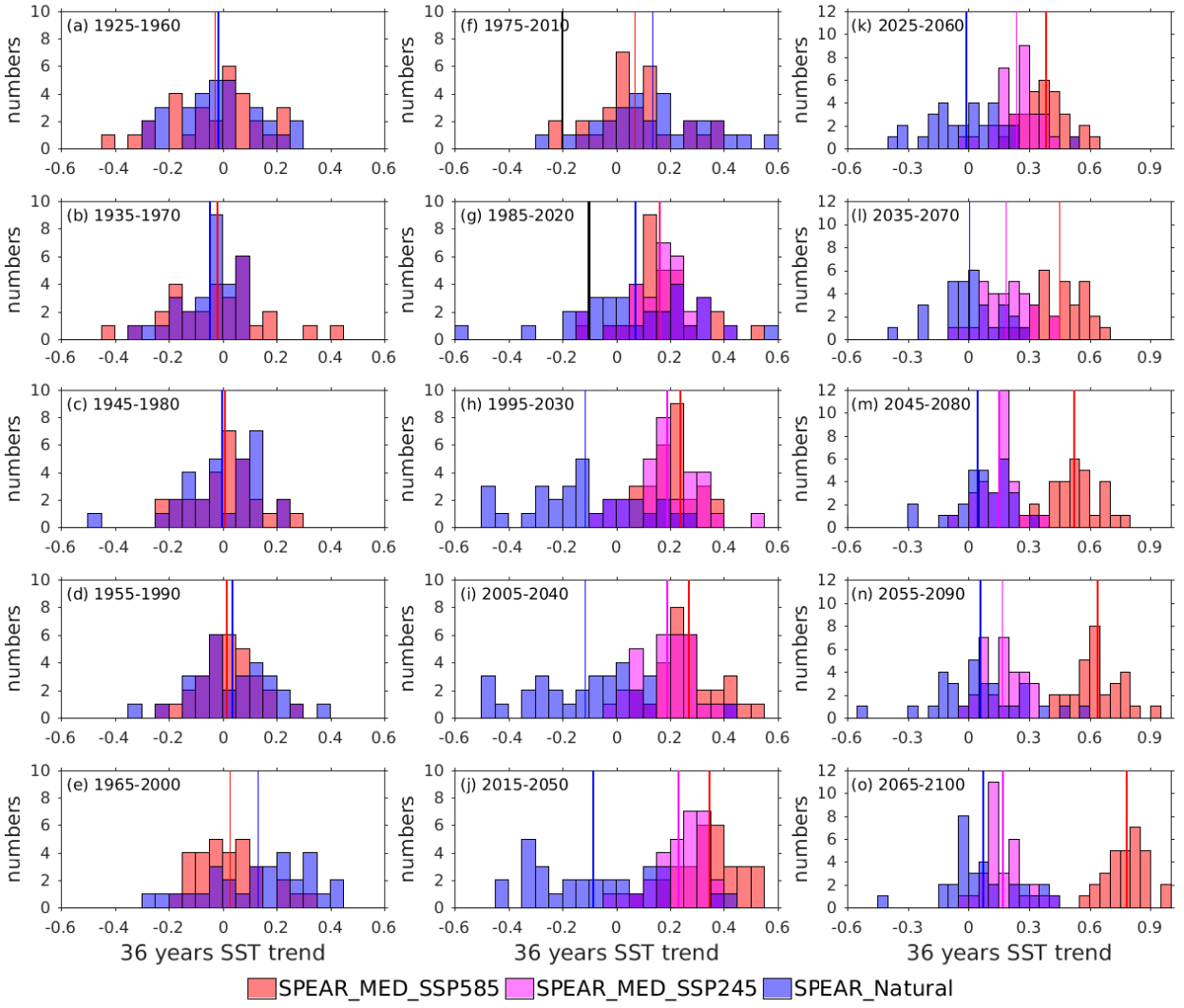

FIG. 7. The histograms of 36-yr annual mean SO SST trend [°C (36 yr)$^{-1}$] in SPEAR_MED_SSP585 (red), SPEAR_MED_SSP245 (magenta), and SPEAR_MED_Natural (blue) large ensembles. (a)–(o) The 36-yr running window is from years 1925–60 to years 2065–2100, respectively, with a time interval of 10 years. The vertical lines overlapping the bars denote the mean of each ensemble. The black lines in (f) and (g) denote the observed SO (averaged south of 50°S) SST trend from Extended Reconstructed sea surface temperature (ERSST) v5 (Huang et al. 2019).

the inherently stronger convection variability in this model (Fig. 2f). The realism of this internal SO convection variability in the model will be discussed in the last section.

b. Do forced convection changes contribute to the recent SO SST trend?

Figure 6 suggests that the influence of internal SO convection variability on SO SST trend lasts approximately to the time period of 2005–40 in the SSP5–8.5 runs and to 2015–50 in the SSP2–4.5 runs. Before these dates, the convection mean state experiences a rapid decline (~1970–2020) due to anthropogenic forcings (Figs. 3a,c,e). This raises the question: How do anthropogenically forced changes in deep convection alter the recently observed SO SST trend beyond the contribution from internal convection variability? To investigate this, we compare the histograms of the 36-yr annual mean SST trends in the Natural simulations with those in the SPEAR_MED_SSP585 and SPEAR_MED_SSP245 simulations which include twenty-first-century anthropogenic forcings (Fig. 7). These histograms are shown every 36 years starting from year 1925 at 10-yr intervals (1925–60, 1935–70, …, 2065–2100), along with each ensemble mean (blue, yellow, and red lines). In the initial several decades (Figs. 7a–d), the histograms of 36-yr SST trends in Natural run and SSP simulations cannot be clearly separated, and the ensemble mean trends are almost overlapping. This suggests that the 36-yr SST trends during these periods are dominated by internal variability, while the forced variability plays a negligible role. This is consistent with the time series in Fig. 3, which shows a small change in forced signal prior to year 1980.

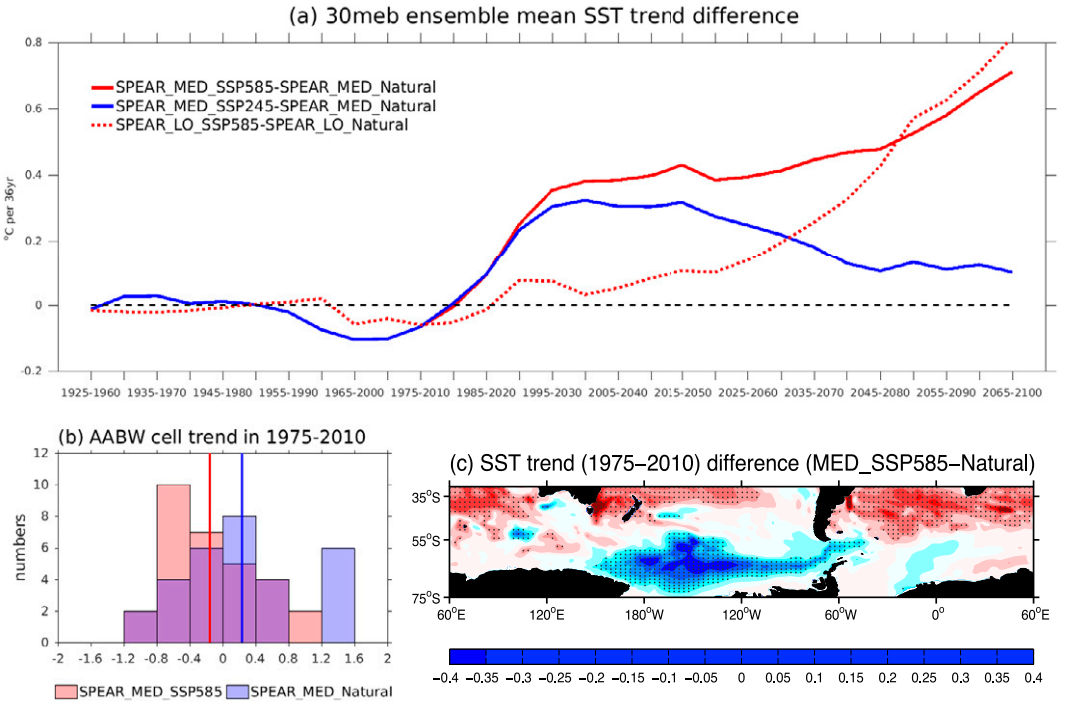

FIG. 8. (a) Differences of ensemble mean 36-yr SO SST trend [°C (36 yr)$^{-1}$] between SPEAR_MED_SSP585 (SPEAR_MED_SSP245; SPEAR_LO_SSP585), and SPEAR_MED_Natural (SPEAR_MED_Natural; SPEAR_LO_Natural). (b) The histograms of AABW cell trend [Sv (36 yr)$^{-1}$; depth space] in 1975–2010 in the SPEAR_MED_SSP585 (red) and SPEAR_MED_Natural (blue) large ensembles. (c) Spatial pattern of ensemble mean SO SST trend differences in the period 1975–2010 between SPEAR_MED_SSP585 and SPEAR_MED_Natural large ensembles. The gray points in (c) denote that the difference is significant at a 95% confidence level based on a Student's *t* test.

In latter time periods, the impact of the forced signal is gradually seen in the histograms. During the 1965–2000 and 1975–2010 time periods (Figs. 7e,f), the ensemble mean SST trend in the SSP simulations is smaller than that in Natural run, although histograms in these runs still overlap substantially. We use a Student's *t* test to examine the significance level of these ensemble mean trend differences and found they are only significant at the 80% confidence level. This suggests that anthropogenic forcing may have affected the 36-yr SST trend in recent decades, but this impact would be difficult to distinguish owing to the dominant role of internal climate variability. The weaker SST trend in the SSP simulations implies that anthropogenic forcing tends to decrease the 36-yr SST trend in recent decades. The observed SO SST trends during the recent periods (1975–2010, 1985–2020) are within the ensemble spread of internal variability, suggesting that the internal variability may not be ignored when attributing the origin of SST trends (Figs. 7f,g). After the time period of 1985–2020 (Figs. 7h–o), the contribution of forced variability increases in strength, acting to increase SST trends. The trends in the histograms for the SSP simulations are significantly different from that in Natural run (99% confidence level), with the trend much warmer in SSP simulations. The warming effect of greenhouse gas forcing appears to play a dominant role during the latter part of the twenty-first century in the SSP simulations.

To highlight the importance of anthropogenic forcing on the SO SST trends, we plot the time evolution of ensemble mean trend differences between the SSP and Natural runs (Fig. 8a). In agreement with Fig. 7, the anthropogenic forcing appears to have little effect in the initial several decades. However, anthropogenic forcing causes a trend reduction in recent decades, and eventually leads to broad warming trends in the twenty-first century. The reduction in trend in recent decades in the simulations is largely associated with anthropogenic forcing–induced convection weakening over the SO. Figure 8b shows the histogram of AABW cell trends in 1975–2010 in both the SSP5–8.5 and Natural runs, along with the ensemble mean trend denoted by vertical lines. The AABW cell trend is more negative in the SSP5–8.5 simulation during this period, which is largely due to the increased precipitation and sea ice melt caused by anthropogenic forcings. The ensemble mean net surface freshwater over the SO shows an increasing trend during this period in the SSP5–8.5 simulation (not shown). This weakened state of SO convection eventually impacts SSTs, particularly around the Ross Sea where the main deep convection occurs (Fig. 8c). We note that the ensemble-mean AABW cell trend difference (computed as SSP5–8.5 minus Natural) is significant at an 85% confidence level, which is slightly higher than the SST trend test, probably due to less noise in the deep ocean variability.

We conduct similar analysis for the SPEAR_LO_SSP585 and SPEAR_LO_Natural. The time evolution of the distributions of SST trends is very similar to SPEAR_MED (not shown). However, the SST trend reduction due to convection weakening in recent decades is smaller than that in SPEAR_MED (Fig. 8a). The trend histograms in SPEAR_LO_Natural and SPEAR_LO_SSP585 in recent decades (e.g., 1975–2010) are harder to distinguish from each other (not shown). However, the ensemble mean surface freshwater increase in SPEAR_LO_SSP585 is comparable to that in SPEAR_MED_SSP585 during recent decades (not shown). This suggests that the forcing difference is not a dominant factor causing these differences. We note that the internal convection variability in SPEAR_LO is much stronger than that in SPEAR_MED (Fig. 2f). This strong internal variability may mask the forced change, particularly during the recent decades when the forced change is not that strong. Given the low significance level in SPEAR_MED and small responses in SPEAR_LO, we can only conclude that the forced convection change due to surface freshwater may partially contribute to the recent SO changes, but many uncertainties remain. It is worth noting, similar to CMIP models, that the models used here do not include freshwater forcing from melting land ice (glacial ice sheets and shelves) over Antarctica. Thus, the impact of convection change due to anthropogenic surface freshening is very likely underestimated in these simulations. The model sensitivity still needs to be considered even with this additional meltwater. Previous studies suggest that Antarctic meltwater can trigger the recent sea ice expansion trend (e.g., Bintanja et al. 2013), while others argue that freshwater from observed melting is not large enough to contribute to the recently observed SO trends even with the meltwater artificially added into the model (e.g., Swart and Fyfe 2013; Pauling et al. 2016). Meanwhile, Bronselaer et al. (2018) pointed out that the meltwater from Antarctic ice sheet and shelves has significant impacts on future climate in addition to recent decades.

c. *What other factors contribute to the SO SST trend and ensemble spread as the SO convection is damped throughout the twenty-first century?*

In later periods of the twenty-first century, the SO convection is strongly damped, including both the mean state and variability (Figs. 3a,c,e). The SO 36-yr SST trends in this period, to the first order, are controlled by the forced anthropogenic warming, particularly in SSP5–8.5 runs, whereas the internal variability represented by the ensemble spreads plays a secondary role (Figs. 3b,d,f). This is in sharp contrast to initial decades when the SST trend is dominated by internal variability. We show in Fig. 9 the SO forced (ensemble mean) SST trends during 2065–2100 to highlight the significant role of the forced signal. The SST trend pattern is characterized by a broad warming over the SO (south of 50°S), although this warming is much weaker than that north of the ACC (Figs. 9a,e,i). As expected, the warming magnitude is reduced in response to smaller radiative forcings in SPEAR_MED_SSP245 (Fig. 9e). Heat budget analysis further confirms that the SO warming trend is largely associated with the surface heat flux term as a result of the greenhouse gas forcing in all runs, whereas the advection and vertical mixing terms play negative roles (Figs. 9b,f,j). In the subsurface ocean, delayed warming in the subpolar SO is clearly seen (Figs. 9d,h,l). Consistent with previous studies (Marshall et al. 2015; Armour et al. 2016; Liu et al. 2018), this north–south warming contrast is primarily due to the anomalous northward heat transport that leads to a heat convergence (divergence) north (south) of the ACC. Moreover, this anomalous northward heat transport is mainly associated with the anomalous heat transport by the mean-state wind-driven MOC (Deacon cell), while the heat transport by the anomalous meridional circulation as a result of the anthropogenic forcing only accounts for ~15%–25% of the total response (Figs. 9c,g,k).

In addition to the first-order anthropogenic warming response mentioned above, we now investigate what other ocean processes may contribute to the spread of SO SST mean state and trend. Since SO convection is very weak during this stage, we speculate that the small convection spread may be primarily a response to other forcing. Figure 4 shows that the AABW cell strength is negatively correlated with the SO SST when SO convection is damped. Here we find that this negative relationship may arise from the SST-related surface freshwater change. Both SPEAR_MED and SPEAR_LO show that ensemble members with higher SO SST favor more freshwater over the surface ocean, eventually contributing to a reduction in AABW cell strength (Figs. 10a–d). We also find the AABW cell and Deacon cell are coupled during this stage. Figure 11 shows that a stronger-than-normal Deacon cell corresponds to a stronger-than-normal AABW cell approximately after the period of 2015–50 in the SSP simulations (SPEAR_MED_SSP585, SPEAR_MED_SSP245, SPEAR_LO_SSP585), in contrast to the overall negative relationships prior to this period. In the Natural run, the relationship between these two cells is persistently negative, suggesting that this negative relationship is internally driven. We also found such negative correlations in the control simulations (not shown). This result is consistent with SO internal deep convection dominating the variability in these simulations or stages. Strong deep ocean convection associated with the strong AABW cell induces a warming of SO SSTs, which decreases the meridional temperature gradient at the ocean surface, weakening the SO westerly jet and thus the Deacon cell strength. Since the extratropical ocean feedback to the atmosphere is very weak (e.g., Zhang et al. 2019), the associated Deacon cell change and its regression coefficient with the AABW cell are relatively weak. On the other hand, when the anthropogenic forcing is strong enough, the internal low-frequency SO convection variability disappears. The damped AABW cell is coupled with the Deacon cell through the enhanced upwelling induced by SO westerlies, or we can say the AABW cell more passively responds to the Deacon cell. This positive correlation between the AABW cell and Deacon cell is also clearly seen in Delworth and Zeng (2008), in which they artificially modify the SO westerly jet in the GFDL CM2.1 model.

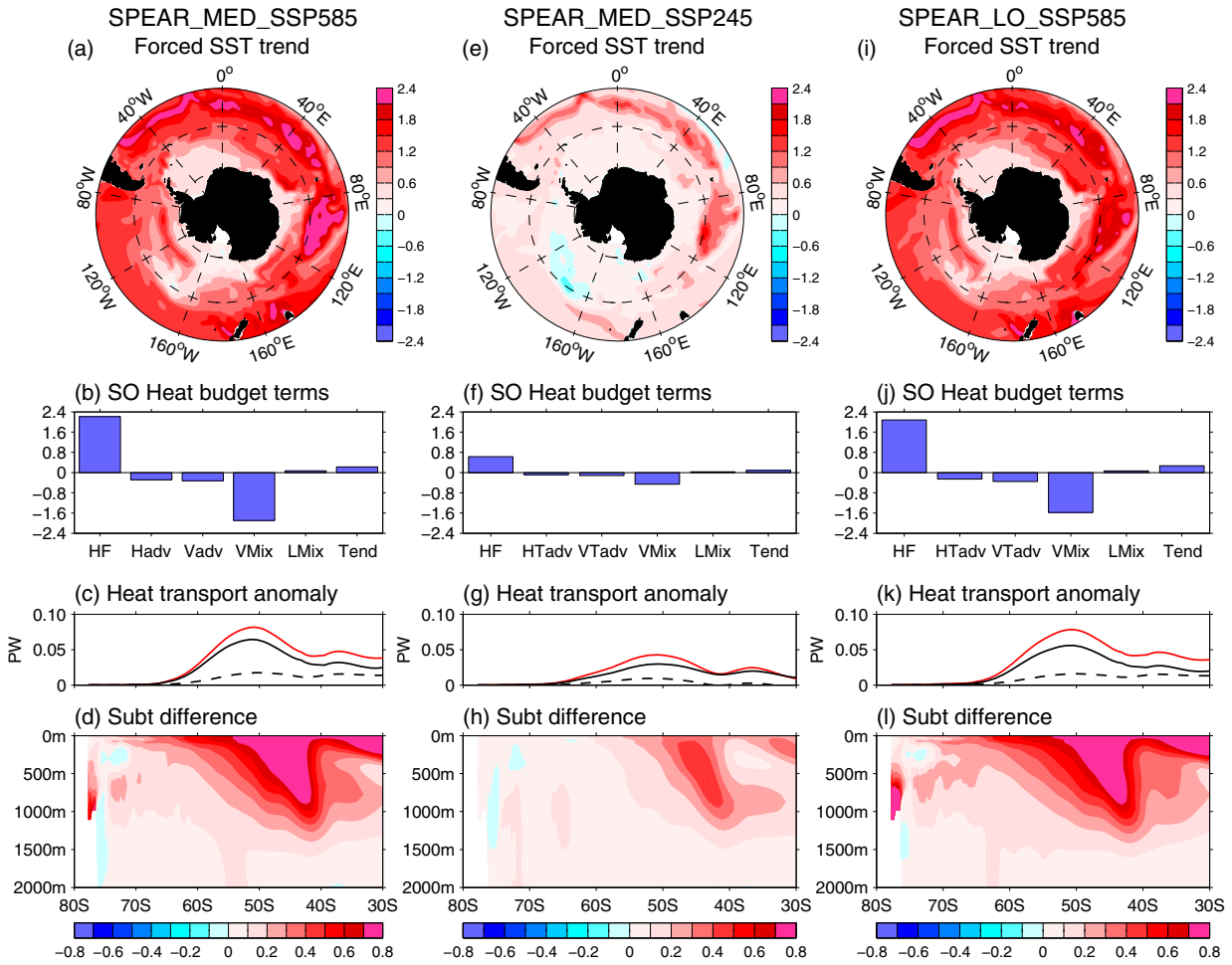

FIG. 9. (a) Spatial pattern of forced ensemble-mean SO SST trend in years 2065–2100 in SPEAR_MED_SSP585. (b) Heat budget analysis of the forced SO area-mean SST difference between years 2083–2100 and 2065–82. The heat budget terms are calculated in the upper 100 m and are averaged south of 50°S. Each term is calculated using instantaneous fields while the model is running, and thus the heat budget is fully closed. HF denotes the tendency from boundary forcing (or surface net heat flux), Hadv the temperature tendency from horizontal advection, Vadv tendency due to vertical advection, VMix the tendency resulting from vertical mixing, LMix the tendency due to lateral (neutral) diffusion, and Tend the overall time tendency. (c) Ocean heat transport difference between years 2083–2100 and 2065–82 (red line: total; black line: heat transport anomaly due to mean MOC $\left(\int\int \overline{v}T'\right)$; dashed black line: heat transport anomaly due to anomalous MOC $\left(\int\int \overline{T}v'\right)$. (d) Zonal-mean ocean temperature difference between years 2083–2100 and 2065–82. (e)–(h) As in (a)–(d), but for the SPEAR_MED_SSP245. (i)–(l) As in (a)–(d), but for the SPEAR_LO_SSP585. Units are °C (36 yr)$^{-1}$ for the SST trend, 0.01 W m^{-2} for the heat tendency term, W m^{-2} for the other heat budget terms, PW for the anomalous ocean heat transport, and °C for the ocean temperature.

Given the positive relationship between the AABW cell and the Deacon cell in later periods of the twenty-first century, we speculate that the negative relationship between the AABW cell and SO SST (Fig. 4) may come from the negative correlation between Deacon cell strength and subpolar SO SST. After all the AABW cell is very weak, while the Deacon cell is quite strong due to strong westerly responses to anthropogenic forcings during this stage (e.g., Solomon and Polvani 2016). This hypothesis is supported by Figs. 12a and 12b that indeed show the ensemble members with a stronger-than-normal Deacon cell corresponding to a cooler-than-normal subpolar SO SST. Figure 12c further points out that the stronger-than-normal Deacon cell is associated with an anomalous northward heat transport that causes a heat convergence (divergence) north (south) of the ACC. This anomalous heat transport eventually leads to a warming anomaly north of the ACC and a cooling anomaly in the subpolar SO (Fig. 12d). Note that the subsurface temperature anomaly south of 60°S is cooler than that in the surface ocean (Fig. 12d), indicating a stronger-than-normal AABW cell (positive response to the spinup of the Deacon cell). However, this AABW cell response is very weak given the strong damping of anthropogenic forcing

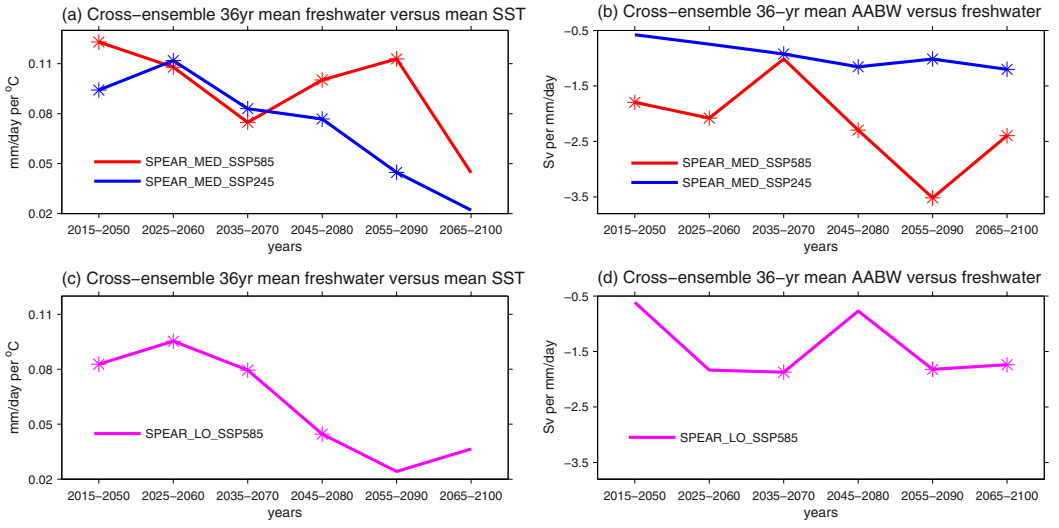

FIG. 10. (a) Cross-ensemble regression of 36-yr mean SO area mean surface freshwater flux upon the 36-yr mean SO area mean SST (mm day^{-1} °C^{-1}) in SPEAR_MED_SSP585 (red line) and SPEAR_MED_SSP245 (blue line). This 36-yr window starts from years 2015–50 and ends in 2065–2100 with a time internal of 10 years. (b) As in (a), but for the regression of AABW cell strength against SO surface freshwater flux [Sv (mm day^{-1})$^{-1}$]. (c),(d) As in (a) and (b), but for the SPEAR_LO_SSP585 large ensemble. The asterisks indicate the regressions are significant at a 90% confidence level based on a Student's *t* test.

as mentioned above. Thus, its associated surface warming cannot overwhelm the divergent cooling caused by an enhanced Deacon cell. We also see that the Deacon cell change contributes to the ensemble spread of the SO SST trend. Figures 13a and 13b illustrate that an ensemble member with a greater strengthening of the Deacon cell corresponds to a more negative 36-yr SST trend in the subpolar SO, which mainly arises from the larger-than-normal heat divergence over the SO (not shown). This is physically consistent with Figs. 9c, 9g, and 9k, which show that the northward heat transport by an anomalous spinup of the Deacon cell contributes positively to the 36-yr SO SST trend, although its magnitude is much smaller than the role

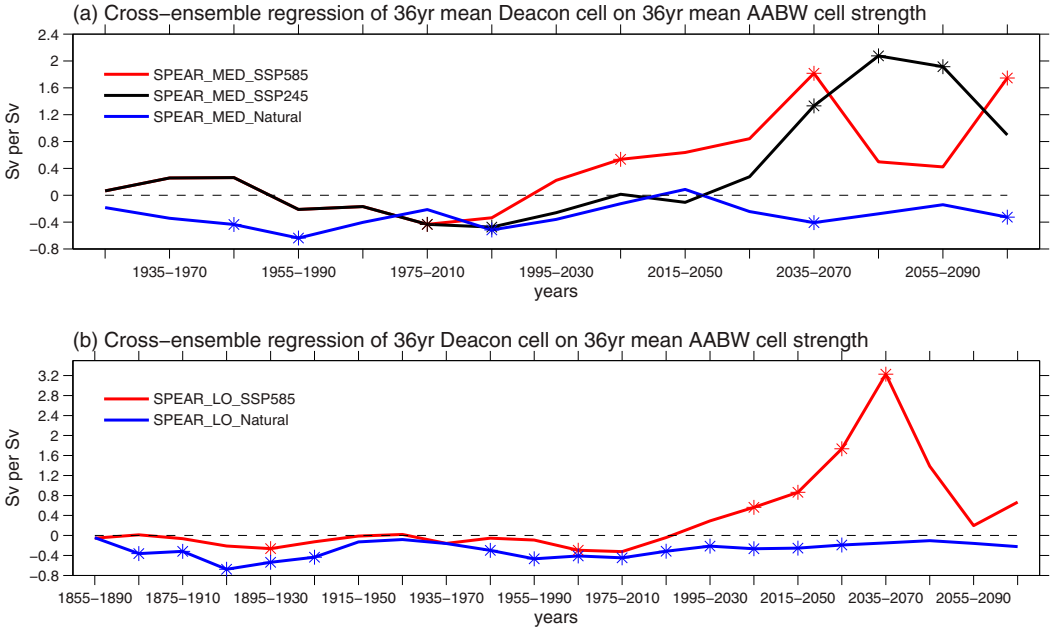

FIG. 11. As in Fig. 4, but for the cross-ensemble regression of 36-yr mean Deacon cell strength on the 36-yr mean AABW cell strength (Sv Sv^{-1}).

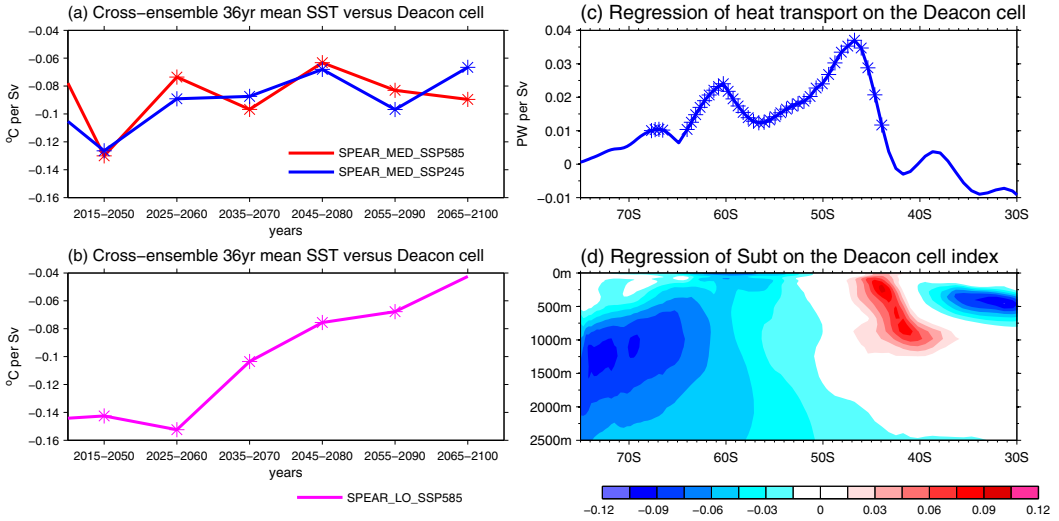

FIG. 12. (a),(b) As in Figs. 10a and 10b, but for the cross-ensemble regression of 36-yr mean SO area-mean SST on the 36-yr mean Deacon cell strength (°C Sv^{-1}). (c) Cross-ensemble regression of ocean heat transport (averaged in years 2065–2100) against the Deacon cell strength (averaged in years 2065–2100) (PW Sv^{-1}). (d) Cross-ensemble regression of zonal mean temperature (averaged in years 2065–2100) against the Deacon cell strength (averaged in years 2065–2100) (°C Sv^{-1}).

of mean-state Deacon cell strength. It is worth noting that the model used here only has a ~0.5° (30 km) resolution around the SO. The model has implemented the Gent–McWilliams parameterization scheme (Gent and Danabasoglu 2011); however, the neutral diffusion and eddy-induced advection are still underestimated compared to eddy-resolving ocean models (Griffies et al. 2015). The Deacon cell response to SO westerly is very likely overestimated due to this underestimation of eddy compensation (e.g., Morrison and Hogg 2013; Griffies et al. 2015), which acts to reduce the isopycnal gradients induced by the increased surface wind stress forcing. It is important to assess the robustness of these results in the future using more advanced parameterization schemes or a high-resolution model that can better resolve ocean eddies.

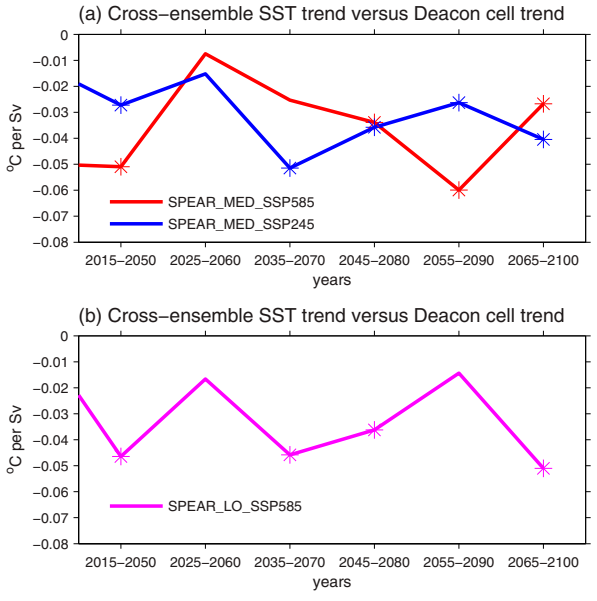

FIG. 13. As in Figs. 10a and 10b, but for the cross-ensemble regression of 36-yr SO SST trend on the 36-yr Deacon cell trend (°C Sv^{-1}).

5. Results in other models

We also analyzed NCAR CESM1 large ensembles (Kay et al. 2015) to examine different roles of the SO MOC in contributing to the observed SO SST trends. We find the SO AABW cell is very weak due to a strongly stratified ocean in its mean state and plays a small role in the 36-yr SO SST trend, even in the initial several decades of the simulations. As shown in Fig. 14a, the relationship between the 36-yr mean AABW cell and the Deacon cell is persistently positive throughout years 1920–2100, in sharp contrast to that in SPEAR (Fig. 11). This suggests that SO convection does not play a dominant role in the SO responses in this model. Instead, it more passively responds to the Deacon cell through upwelling drag by the SO westerly changes. The roles of the Deacon cell in the SO mean SST and SST trend are clearly seen in this model (Fig. 14b). The Deacon cell spread is negatively correlated with the SO SST spread throughout years 1920–2100, no matter the mean state or trend, due to an anomalous meridional heat transport divergence.

We also checked previous GFDL large ensembles based on the SPEAR_AM2 (Zhang et al. 2019) and FLOR (Vecchi et al. 2014) models. The SO convection variability in these two models is also very strong and fluctuates on multidecadal time scales. As expected, the influence of internal AABW cell

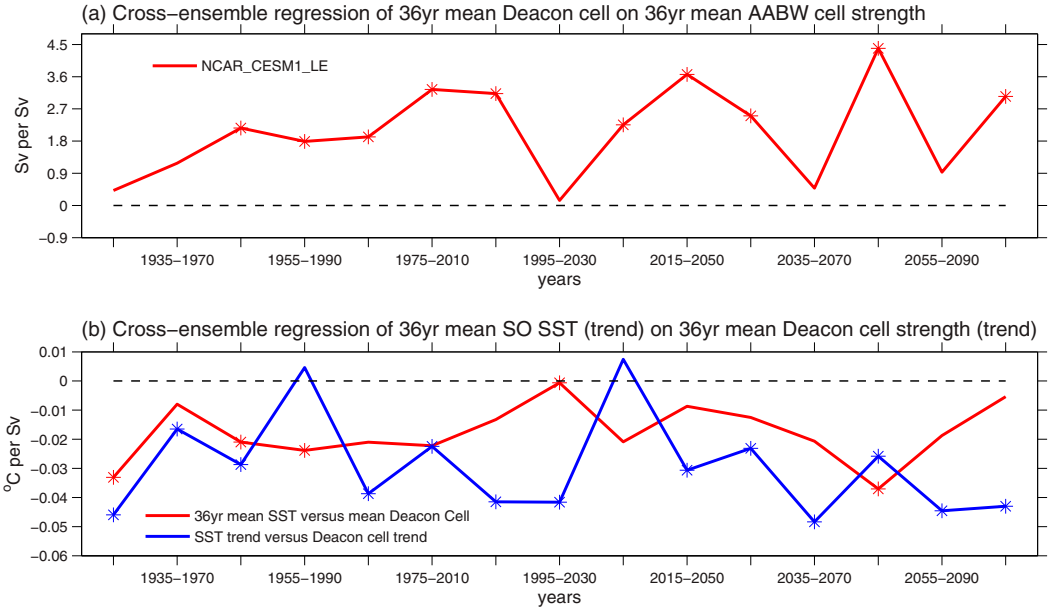

FIG. 14. (a) As in Fig. 10, but for the cross-ensemble regression of 36-yr mean Deacon cell strength on the 36-yr mean AABW cell strength in NCAR_CESM1_LE model (Sv Sv^{-1}). (b) Cross-ensemble regression (°C Sv^{-1}) of 36-yr mean SO area mean SST on the 36-yr mean Deacon cell strength (red line) and 36-yr SO SST trend upon the 36-yr Deacon cell strength trend (blue line) in the NCAR_CESM1_LE model.

variability on the SO 36-yr SST trend is clearly seen in both models, with positive (negative) relationships between the AABW trend (initial AABW state) and SST trend (Figs. 15a,b). In contrast to SPEAR_LO_SSP585 and SPEAR_MED_SSP585, the roles of internal convection variability in the SPEAR_AM2 and FLOR models are not damped by anthropogenic forcing and they last through the end of the twenty-first century (Fig. 6 vs Figs. 15a,b). Figure 16 shows that the mean convection is damped by anthropogenic forcing, while the low-frequency convection variability still remains into the twenty-first century. This low-frequency variability then imprints on the SO SST trend and becomes a dominant factor in the ensemble spread of the trend. To first order, the SO SST trend in the last several decades of the twenty-first century is still dominated by the forced warming trend due to radiative forcings, similar to SPEAR_LO_SSP585 and SPEAR_MED_SSP585. To second order, the internal convection variability contributes mostly to the ensemble spread of the SO SST trend. The physical processes determining these differences in the SO convection response to anthropogenic forcing need to be investigated further.

6. Summary

One of the most puzzling features of climate change over the last several decades is the cooling trend of SSTs and associated expansion of Antarctic sea ice in the subpolar SO. In this paper, we explored the possible roles that SO meridional overturning circulation (MOC) plays in contributing to these observed trends using large ensembles of climate model simulations. We find that from the late nineteenth through twenty-first century different physical processes associated with the MOC can play strong roles in determining interdecadal-scale SST trends that are similar to observed trends. The GFDL models typically have relatively active deep ocean convection in the SO, as well as distinct multidecadal variability of the strength of that convection. When forced by time-evolving historical radiative forcings and projections of future radiative forcing changes, this low-frequency convection variability can induce similar time scale variations of SO SST, at least in the nineteenth through early twenty-first centuries. Ensemble members with initial stronger-than-normal SO convection experience more negative SST trends in the subsequent 36 years as a result of convection weakening, consistent with the arguments in Zhang et al. (2019). During recent decades, anthropogenic forcing joins internal variability as a major factor in the simulated SO SST trends. Weakened forced convection due to surface freshening may also contribute to this trend (e.g., Bintanja et al. 2013; Swart and Fyfe 2013; Pauling et al. 2016). Later in the twenty-first century, the anthropogenic forcing is very strong and damps the SO convection mean state and its low-frequency variability. The SO SST trend during this stage is dominated by the forced anthropogenic warming, while the meridional SST trend contrast separated by the ACC can be explained by an anomalous northward heat transport by the mean-state wind-driven Deacon cell (e.g., Armour et al. 2016).

Our study here suggests that the previous three hypotheses used to explain the observed SO cooling SST trend (natural

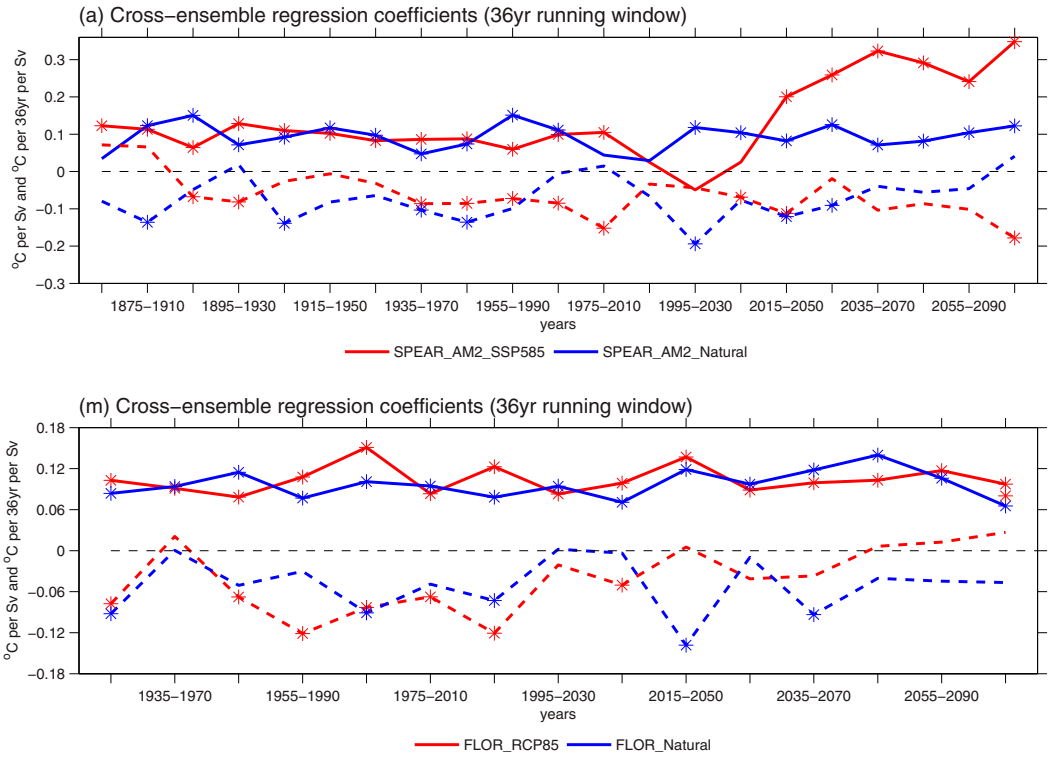

FIG. 15. As in Fig. 6, but for the SPEAR_AM2 and FLOR large ensembles.

variability of SO convection, radiatively forced weakening of SO convection variability, and role of SO mean MOC) can all be present in a single model. Different processes can control the SO SST trend during different periods in GFDL climate models. In other words, different processes can be dominant depending on overall conditions. When anthropogenic forcing is weak, natural variability of convection can be a dominant factor assuming that the natural variability of convection is strong enough, as seen in Zhang et al. (2019). The forced convection weakening could also contribute somewhat to the SO SST trend, as long as the freshwater fluxes are strong enough, particularly when adding the meltwater of Antarctic ice sheets and shelves. This indeed occurs in some modeling studies (e.g., Bintanja et al. 2013; Bronselaer et al. 2018). As SO convection is damped by anthropogenic forcings, the Deacon cell starts to play a progressively larger role. Thus, it is not

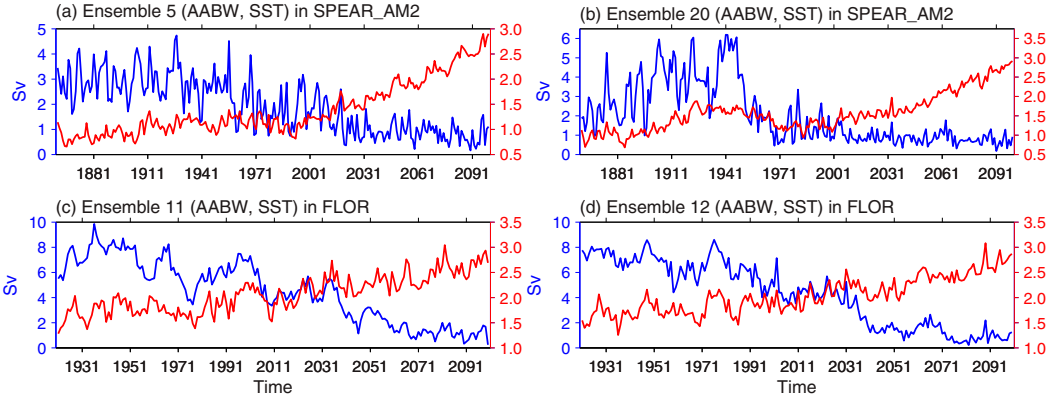

FIG. 16. Time evolutions of the AABW cell (in depth space; Sv; blue line) and SO area mean SST (°C; red line) in ensemble members (a) 5 and (b) 20 in the SPEAR_AM2 large ensemble. (c),(d) As in (a) and (b), but for the ensemble members 11 and 12, respectively, in the FLOR large ensemble.

surprising to see a significant impact of Deacon cell modulation on SO SST in models without strong convection variability, such as the MITGCM and NCAR CESM models (e.g., Marshall et al. 2015; Armour et al. 2016; Liu et al. 2018).

In the observation, different processes may dominate in different periods and multiple processes may be at work in one period. After the observed 1974–76 Weddell Polynya, the abyssal (surface) ocean is very likely to have experienced warming (cooling) and salinification (freshening) (e.g., Zanowski et al. 2015; Zhang et al. 2019) due to its persistence. This weakening of open ocean deep convection may covary with the anthropogenic forced convection weakening, which can lead to a stronger-than-normal convection weakening between the 1980s and 2000s that favors a cooling SO SST trend. The Deacon cell is also very likely to work together with this convection weakening. As shown in Fig. 9 and in previous studies (e.g., Armour et al. 2016), the anomalous northward heat transport by the mean Deacon cell can only explain the meridional SST trend contrast, rather than the real SO cooling trend. The more realistic surface and subsurface SO states can be obtained when we take into consideration the SO convection weakening due to both anthropogenic forcing and internal variability. Improved and sustained measurements of the subsurface ocean—particularly the MLD evolutions around the Ross and Weddell Seas, and the heat storage changes north of the ACC—could help determine the state of the real SO system (convecting, nonconvecting, or advecting heat) during different epochs.

The GFDL SPEAR and FLOR are "convecting" models, which offer a glimpse into how the SO behaves in the presence of low-frequency convection variability. Given the sparse observations over the SO, it is difficult to determine whether this low-frequency convection variability is realistic. Zhang et al. (2021) examined Antarctic paleoclimate records and found that the surface air temperature displays a ~150-yr oscillation over most of the continent. Goosse et al. (2021) further pointed out that large open ocean polynyas, like the observed 1974–76 Weddell Polynya, are rare events in the past climate, and have occurred at most a few times per century. These studies suggest that low-frequency convection variability has likely occurred in the past climate. However, Zhang et al. (2021) also suggested that the SPEAR_LO may overestimate the amplitude of this low-frequency variability relative to paleoclimate records. Thus, it remains unclear to what extent low-frequency variability imprints on the recent SO SST trends and how this variability may evolve under anthropogenic forcing. The SPEAR and FLOR simulations offer two possibilities: damped versus sustained variability. Lockwood et al. (2021) pointed out that the Antarctic Slope Current (ASC) determines whether the model simulates continued SO deep convection versus no convection as climate warms. This suggests that SO convection may be able to exert a stronger influence later in the twenty-first century in models that are able to resolve ASC dynamics. We also note that different models may have different convection sites (e.g., Mohrmann et al. 2021), which can lead to different SST spatial patterns as convection weakens, even in models with a similar SO area-averaged SST change. Although we only examine the roles of the SO MOC in the SO SST trend, additional processes, particularly related to the atmosphere and sea ice (surface winds and storms and the drift, advection, and freshwater transport of sea ice), could also play a role. Those processes are very important to the spatial pattern of the SST trend and are critical to polynya events in some periods (e.g., Meehl et al. 2016; Haumann et al. 2016; Lee et al. 2017; Campbell et al. 2019). A wide variety of factors must be considered to better understand the observed changes and their implications for future behavior.

Acknowledgments. We are grateful to Pu Lin and Matthew Harrison, who provided extremely insightful and valuable feedback and suggestions, for their constructive comments on an early version of the paper. This work is supported as a base activity of NOAA's Geophysical Fluid Dynamics Laboratory (GFDL) and supported by University Corporation for Atmospheric Research (UCAR) and Princeton University under block funding from NOAA/GFDL.

Data availability statement. Data used in this study are available upon request.

REFERENCES

Adcroft, A., and Coauthors, 2019: The GFDL global ocean and sea ice model OM4.0: Model description and simulation features. *J. Adv. Model. Earth Syst.*, **11**, 3167–3211, https://doi.org/10.1029/2019MS001726.

Anderson, J. L., and Coauthors, 2004: The new GFDL global atmosphere and land model AM2–LM2: Evaluation with prescribed SST simulations. *J. Climate*, **17**, 4641–4673, https://doi.org/10.1175/JCLI-3223.1.

Armour, K. C., J. Marshall, J. Scott, A. Donohoe, and E. R. Newsom, 2016: Southern Ocean warming delayed by circumpolar upwelling and equatorward transport. *Nat. Geosci.*, **9**, 549–555, https://doi.org/10.1038/ngeo2731.

Bilgen, S. I., and B. P. Kirtman, 2020: Impact of ocean model resolution on understanding the delayed warming of the Southern Ocean. *Environ. Res. Lett.*, **15**, 114012, https://doi.org/10.1088/1748-9326/abbc3e.

Bintanja, R., G. J. van Oldenborgh, S. S. Drijfhout, B. Wouters, and C. A. Katsman, 2013: Important role for ocean warming and increased ice-shelf melt in Antarctic sea ice expansion. *Nat. Geosci.*, **6**, 376–379, https://doi.org/10.1038/ngeo1767.

Bronselaer, B., and Coauthors, 2018: Change in future climate due to Antarctic meltwater. *Nature*, **564**, 53–58, https://doi.org/10.1038/s41586-018-0712-z.

Campbell, E. C., E. A. Wilson, G. W. K. Moore, S. C. Riser, C. E. Brayton, M. R. Mazloff, and L. D. Talley, 2019: Antarctic offshore polynyas linked to Southern Hemisphere climate anomalies. *Nature*, **570**, 319–325, https://doi.org/10.1038/s41586-019-1294-0.

Chemke, R., and L. M. Polvani, 2020: Using multiple large ensembles to elucidate the discrepancy between the 1979–2019 modeled and observed Antarctic sea ice trends. *Geophys. Res. Lett.*, **47**, e2020GL088339, https://doi.org/10.1029/2020GL088339.

Cheon, W. G., and A. L. Gordon, 2019: Open-ocean polynyas and deep convection in the Southern Ocean. *Sci. Rep.*, **9**, 6935, https://doi.org/10.1038/s41598-019-43466-2.

de Lavergne, C., J. B. Palter, E. D. Galbraith, R. Bernardello, and I. Marinov, 2014: Cessation of deep convection in the open Southern Ocean under anthropogenic climate change. *Nat. Climate Change*, **4**, 278–282, https://doi.org/10.1038/nclimate2132.

Delworth, T. L., and F. Zeng, 2008: Simulated impact of altered Southern Hemisphere winds on the Atlantic meridional overturning circulation. *Geophys. Res. Lett.*, **35**, L20708, https://doi.org/10.1029/2008GL035166.

——, and Coauthors, 2006: GFDL's CM2 global coupled climate models. Part I: Formulation and simulation characteristics. *J. Climate*, **19**, 643–674, https://doi.org/10.1175/JCLI3629.1.

——, and Coauthors, 2012: Simulated climate and climate change in the GFDL CM2.5 high-resolution coupled climate model. *J. Climate*, **25**, 2755–2781, https://doi.org/10.1175/JCLI-D-11-00316.1.

——, and Coauthors, 2020: SPEAR-the next generation GFDL modeling system for seasonal to multidecadal prediction and projection. *J. Adv. Model. Earth Syst.*, **12**, e2019MS001895, https://doi.org/10.1029/2019MS001895.

Eyring, V., S. Bony, G. A. Meehl, C. A. Senior, B. Stevens, R. J. Stouffer, and K. E. Taylor, 2016: Overview of the Coupled Model Intercomparison Project Phase 6 (CMIP6) experimental design and organization. *Geosci. Model Dev.*, **9**, 1937–1958, https://doi.org/10.5194/gmd-9-1937-2016.

Ganachaud, A., and C. Wunsch, 2000: Improved estimates of global ocean circulation, heat transport and mixing from hydrographic data. *Nature*, **408**, 453–457, https://doi.org/10.1038/35044048.

Gent, P. R., and G. Danabasoglu, 2011: Response to increasing Southern Hemisphere winds in CCSM4. *J. Climate*, **24**, 4992–4998, https://doi.org/10.1175/JCLI-D-10-05011.1.

Goosse, H., Q. Dalaiden, M. G. P. Cavitte, and L. Zhang, 2021: Can we reconstruct the formation of large open ocean polynyas in the Southern Ocean using ice core records? *Climate Past*, **17**, 111–131, https://doi.org/10.5194/cp-17-111-2021.

Gordon, A. L., 1978: Deep Antarctic convection west of Maud Rise. *J. Phys. Oceanogr.*, **8**, 600–612, https://doi.org/10.1175/1520-0485(1978)008<0600:DACWOM>2.0.CO;2.

Griffies, S. M., and Coauthors, 2015: Impacts on ocean heat from transient mesoscale eddies in a hierarchy of climate models. *J. Climate*, **28**, 952–977, https://doi.org/10.1175/JCLI-D-14-00353.1.

Haumann, F. A., N. Gruber, M. Münnich, I. Frenger, and S. Kern, 2016: Sea-ice transport driving Southern Ocean salinity and its recent trends. *Nature*, **537**, 89–92, https://doi.org/10.1038/nature19101.

He, J., M. Winton, G. Vecchi, L. Jia, and M. Rugenstein, 2017: Transient climate sensitivity depends on base climate ocean circulation. *J. Climate*, **30**, 1493–1504, https://doi.org/10.1175/JCLI-D-16-0581.1.

Holland, P. R., and R. Kwok, 2012: Wind-driven trends in Antarctic sea-ice drift. *Nat. Geosci.*, **5**, 872–875, https://doi.org/10.1038/ngeo1627.

Huang, B., C. Liu, G. Ren, H.-M. Zhang, and L. Zhang, 2019: The role of buoy and Argo observations in two SST analyses in the global and tropical Pacific oceans. *J. Climate*, **32**, 2517–2535, https://doi.org/10.1175/JCLI-D-18-0368.1.

Kay, J. E., and Coauthors, 2015: The Community Earth System Model (CESM) Large Ensemble Project: A community resource for studying climate change in the presence of internal climate variability. *Bull. Amer. Meteor. Soc.*, **96**, 1333–1349, https://doi.org/10.1175/BAMS-D-13-00255.1.

Kim, W. M., S. Yeager, P. Chang, and G. Danabasoglu, 2018: Low-frequency North Atlantic climate variability in the Community Earth System Model large ensemble. *J. Climate*, **31**, 787–813, https://doi.org/10.1175/JCLI-D-17-0193.1.

Lee, S.-K., D. Volkov, H. Lopez, W. G. Cheon, A. L. Gordon, Y. Liu, and R. Wanninkhof, 2017: Wind-driven ocean dynamics impact on the contrasting sea-ice trends around West Antarctica. *J. Geophys. Res. Oceans*, **122**, 4413–4430, https://doi.org/10.1002/2016JC012416.

Li, X., D. M. Holland, E. P. Gerber, and C. Yoo, 2014: Impacts of the north and tropical Atlantic Ocean on the Antarctic Peninsula and sea ice. *Nature*, **505**, 538–542, https://doi.org/10.1038/nature12945.

Liu, W., J. Lu, S.-P. Xie, A. Fedorov, W. Liu, J. Lu, S.-P. Xie, and A. Fedorov, 2018: Southern Ocean heat uptake, re-distribution, and storage in a warming climate: The role of meridional overturning circulation. *J. Climate*, **31**, 4727–4743, https://doi.org/10.1175/JCLI-D-17-0761.1.

Lockwood, J. W., C. O. Dufour, S. M. Griffies, and M. Winton, 2021: On the role of the Antarctic Slope Front on the occurrence of the Weddell Sea polynya under climate change. *J. Climate*, **34**, 2529–2548, https://doi.org/10.1175/JCLI-D-20-0069.1.

Lumpkin, R., and K. Speer, 2007: Global ocean meridional overturning. *Phys. Oceanogr.*, **37**, 2550–2562, https://doi.org/10.1175/JPO3130.1.

Marshall, J., and K. Speer, 2012: Closure of the meridional overturning circulation through Southern Ocean upwelling. *Nat. Geosci.*, **5**, 171–180, https://doi.org/10.1038/ngeo1391.

——, J. R. Scott, K. C. Armour, J.-M. Campin, M. Kelley, and A. Romanou, 2015: The ocean's role in the transient response of climate to abrupt greenhouse gas forcing. *Climate Dyn.*, **44**, 2287–2299, https://doi.org/10.1007/s00382-014-2308-0.

Martinson, D. G., 1991: Open ocean convection in the Southern Ocean. *Deep Convection and Deep Water Formation in the Oceans.* J. C. Gascard and P. C. Chu, Eds., Elsevier, 37–52.

Meehl, G. A., J. M. Arblaster, C. M. Bitz, C. T. Y. Chung, and H. Teng, 2016: Antarctic sea-ice expansion between 2000 and 2014 driven by tropical Pacific decadal climate variability. *Nat. Geosci.*, **9**, 590–595, https://doi.org/10.1038/ngeo2751.

Mohrmann, M., C. Heuzé, and S. Swart, 2021: Southern Ocean polynyas in CMIP6 models. *Cryosphere Discuss.*, **15**, 4281–4313, https://doi.org/10.5194/tc-15-4281-2021.

Morrison, A. K., and A. M. Hogg, 2013: On the relationship between Southern Ocean overturning and ACC transport. *J. Phys. Oceanogr.*, **43**, 140–148, https://doi.org/10.1175/JPO-D-12-057.1.

Orsi, A. H., G. C. Johnson, and J. L. Bullister, 1999: Circulation, mixing, and production of Antarctic Bottom Water. *Prog. Oceanogr.*, **43**, 55–109, https://doi.org/10.1016/S0079-6611(99)00004-X.

Parkinson, C. L., 2019: A 40-y record reveals gradual Antarctic sea ice increases followed by decreases at rates far exceeding the rates seen in the Arctic. *Proc. Natl. Acad. Sci. USA*, **116**, 14 414–14 423, https://doi.org/10.1073/pnas.1906556116.

Pauling, A. G., C. M. Bitz, I. J. Smith, and P. J. Langhorne, 2016: The response of the Southern Ocean and Antarctic sea ice to freshwater from ice shelves in an Earth system model. *J. Climate*, **29**, 1655–1672, https://doi.org/10.1175/JCLI-D-15-0501.1.

Polvani, L. M., and K. L. Smith, 2013: Can natural variability explain observed Antarctic sea ice trends? New modeling evidence from CMIP5. *Geophys. Res. Lett.*, **40**, 3195–3199, https://doi.org/10.1002/grl.50578.

Purich, A., and Coauthors, 2016: Tropical Pacific SST drivers of recent Antarctic sea ice trends. *J. Climate*, **29**, 8931–8948, https://doi.org/10.1175/JCLI-D-16-0440.1.

Purkey, S. G., and G. C. Johnson, 2012: Global contraction of Antarctic Bottom Water between the 1980s and 2000s. *J. Climate*, **25**, 5830–5844, https://doi.org/10.1175/JCLI-D-11-00612.1.

——, and ——, 2013: Antarctic Bottom Water warming and freshening: Contributions to sea level rise, ocean freshwater budgets, and global heat gain. *J. Climate*, **26**, 6105–6122, https://doi.org/10.1175/JCLI-D-12-00834.1.

Riahi, K., and Coauthors, 2017: The shared socioeconomic pathways and their energy, land use, and greenhouse gas emissions implications: An overview. *Global Environ. Change*, **42**, 153–168, https://doi.org/10.1016/j.gloenvcha.2016.05.009.

Roach, L. A., and Coauthors, 2020: Antarctic sea ice area in CMIP6. *Geophys. Res. Lett.*, **47**, e2019GL086729, https://doi.org/10.1029/2019GL086729.

Russell, J. L., D. W. Dixon, A. Gnanadesikan, R. J. Stouffer, and J. R. Toggweiler, 2006: The Southern Hemisphere westerlies in a warming world: Propping open the door to the deep ocean. *J. Climate*, **19**, 6382–6390, https://doi.org/10.1175/JCLI3984.1.

Sigman, D. M., and E. A. Boyle, 2000: Glacial/interglacial variations in atmospheric carbon dioxide. *Nature*, **407**, 859–869, https://doi.org/10.1038/35038000.

Singh, H., L. Polvani, and P. Rasch, 2019: Antarctic sea ice expansion, driven by internal variability, in the presence of increasing atmospheric CO_2. *Geophys. Res. Lett.*, **46**, 14 762–14 771, https://doi.org/10.1029/2019GL083758.

Solomon, A., and L. M. Polvani, 2016: Highly significant responses to anthropogenic forcings of the midlatitude jet in the Southern Hemisphere. *J. Climate*, **29**, 3463–3470, https://doi.org/10.1175/JCLI-D-16-0034.1.

Swart, N. C., and J. C. Fyfe, 2013: The influence of recent Antarctic ice sheet retreat on simulated sea ice area trends. *Geophys. Res. Lett.*, **40**, 4328–4332, https://doi.org/10.1002/grl.50820.

Turner, J., and Coauthors, 2009: Non-annular atmospheric circulation change induced by stratospheric ozone depletion and its role in the recent increase of Antarctic sea ice extent. *Geophys. Res. Lett.*, **36**, L08502, https://doi.org/10.1029/2009GL037524.

——, J. S. Hosking, T. J. Bracegirdle, G. J. Marshall, and T. Phillips, 2015: Recent changes in Antarctic sea ice. *Philos. Trans. Roy. Soc. London*, **A373**, 20140163, https://doi.org/10.1098/rsta.2014.0163.

Vecchi, G., and Coauthors, 2014: On the seasonal forecasting of regional tropical cyclone activity. *J. Climate*, **27**, 7994–8016, https://doi.org/10.1175/JCLI-D-14-00158.1.

Wang, C., L. Zhang, S.-K. Lee, L. Wu, and C. R. Mechoso, 2014: A global perspective on CMIP5 climate model biases. *Nat. Climate Change*, **4**, 201–205, https://doi.org/10.1038/nclimate2118.

Zanowski, H., R. Hallberg, and J. L. Sarmiento, 2015: Abyssal ocean warming and salinification after Weddell polynyas in the GFDL CM2G coupled climate model. *J. Phys. Oceanogr.*, **45**, 2755–2772, https://doi.org/10.1175/JPO-D-15-0109.1.

Zhang, L., and T. L. Delworth, 2016: Impact of the Antarctic bottom water formation on the Weddell Gyre and its northward propagation characteristics in GFDL model. *J. Geophys. Res. Oceans*, **121**, 5825–5846, https://doi.org/10.1002/2016JC011790.

——, ——, and L. Jia, 2017: Diagnosis of decadal predictability of Southern Ocean sea surface temperature in the GFDL CM2.1 model. *J. Climate*, **30**, 6309–6328, https://doi.org/10.1175/JCLI-D-16-0537.1.

——, ——, W. Cooke, and X. Yang, 2019: Natural variability of Southern Ocean convection as a driver of observed climate trends. *Nat. Climate Change*, **9**, 59–65, https://doi.org/10.1038/s41558-018-0350-3.

——, ——, ——, H. Goosse, M. Bushuk, Y. Morioka, and X. Yang, 2021: The dependence of internal multidecadal variability in the Southern Ocean on the ocean background mean state. *J. Climate*, **34**, 1061–1080, https://doi.org/10.1175/JCLI-D-20-0049.1.

Zhang, R., 2010: Latitudinal dependence of Atlantic meridional overturning circulation (AMOC) variations. *Geophys. Res. Lett.*, **37**, L16703, https://doi.org/10.1029/2010GL044474.

Zhao, M., and Coauthors, 2018a: The GFDL global atmosphere and land model AM4.0/LM4.0: 1. Simulation characteristics with prescribed SSTs. *J. Adv. Model. Earth Syst.*, **10**, 691–734, https://doi.org/10.1002/2017MS001208.

——, and Coauthors, 2018b: The GFDL global atmosphere and land model AM4.0/LM4.0: 2. Model description, sensitivity studies, and tuning strategies. *J. Adv. Model. Earth Syst.*, **10**, 735–769, https://doi.org/10.1002/2017MS001209.